

DC SQUID Magnetometry

by

Christopher Bennett Rich

B.Sc., Rice University, 2005

Thesis Submitted in Partial Fulfillment of the
Requirements for the Degree of
Master of Science

in the
Department of Physics
Faculty of Science

© Christopher Bennett Rich 2019
SIMON FRASER UNIVERSITY
Fall 2019

All rights reserved.

However, in accordance with the *Copyright Act of Canada*, this work may be reproduced without authorization under the conditions for “Fair Dealing.” Therefore, limited reproduction of this work for the purposes of private study, research, education, satire, parody, criticism, review and news reporting is likely to be in accordance with the law, particularly if cited appropriately.

Approval

Name: Christopher Bennett Rich
Degree: Master of Science (Physics)
Title: *DC SQUID Magnetometry*
Examining Committee: **Chair:** Malcolm Kennett
Associate Professor

David Broun
Senior Supervisor
Associate Professor

Mohammad Amin
Supervisor
Adjunct Professor

J. Steven Dodge
Internal Examiner
Associate Professor

Date Defended: Thursday 10th October, 2019

Abstract

This thesis describes the measurement of the local magnetic field of a D-Wave Systems Washington generation processor using on-chip multiplexed unshunted DC SQUID magnetometers. These measurements are used in conjunction with passive and active field compensation to minimize the magnetic field present during the superconducting transition of the chip in order to limit the number of magnetic flux lines trapped on chip. This maximizes the operability of the superconducting quantum processor.

Keywords: Simon Fraser University; DC SQUID magnetometer; Trapped magnetic flux mitigation; Unshunted Josephson junction; Multiplex; Superconducting electronics

Dedication

For my family.

Acknowledgements

This thesis is the culmination of many years of work and study. There are many people without whom this thesis would not exist. I would like to acknowledge and thank them.

Prof. David Broun. When I first thought about pursuing a graduate degree while working full time, it wasn't obvious how that process would work. David has been supportive from start to finish and has helped define and navigate that process with me. He has always made himself available, whether it is to discuss cryogenics and superconducting devices, to navigate any administrative hurdles or teach a course on short notice. I couldn't ask for a better advisor.

Dr. Mark Johnson. From the time I first broached the idea of continuing my education, through now, he has been nothing but supportive. He has shown full confidence in me throughout this endeavor, not questioning once could I handle or should I take on the extra workload. Mark has never hesitated to answer any of my questions since I joined D-Wave, during my studies or the writing of this thesis. For that I am grateful.

All of my past and present colleagues at D-Wave Systems. Working at D-Wave was and still is my dream job. My colleagues continue to foster an intellectually stimulating and challenging environment where I am free and encouraged to ask any questions I have. The bulk of my knowledge of cryogenics, superconducting electronics and quantum computing has been gained through my work with my colleagues at D-Wave. We have faced many challenges, encountered fantastic problems and solved them — together. With them, I have achieved the greatest successes of my professional career. I am privileged to call them not just colleagues, but friends.

Dr. Vicki Colvin, Dr. Dan Mittleman and Dr. James Kinsey. My undergraduate research experience solidified my desire to be a professional scientist. In their labs, I experienced what it was like to work in a research lab and was hooked. Equipment would (and did!) break, data could be (and was!) confusing, but it's not magic... it's science. The challenges are surmountable. Don't panic, break the problem down into smaller chunks and start figuring things out. I attribute my success in professional career directly to the invaluable experience I gained in their respective labs. Thank you.

My family. My parents instilled in me the importance of dreaming big. But big dreams are rarely easy. Each time I have pursued those dreams, my family's unwavering support and

encouragement have made those journeys that much easier. When I proclaimed I wanted to move to Canada to build quantum computers, they started packing my car. When the stress from work and school build up, my brother's phone calls cheer me up. I love you all and could not have achieved any of this without your support. This thesis is for you.

Contents

Approval	ii
Abstract	iii
Dedication	iv
Acknowledgements	v
Table of Contents	vii
List of Tables	ix
List of Figures	x
List of Symbols	xi
List of Acronyms	xii
1 Introduction	1
1.1 Superconducting circuits	1
1.2 Flux trapping	2
1.3 Consequences of trapped flux in superconducting processors	3
1.4 Minimizing the effects of trapped flux	5
1.5 Minimizing the trapped flux in wires	6
1.6 Minimizing the amount of trapped flux	6
1.6.1 Low-field cooling	6
1.7 Magnetic field measurement	8
1.7.1 Flux-locked loop DC SQUID	8
1.7.2 Unshunted DC SQUID with I_{sw} modulation	9
2 Theory	10
2.1 Superconducting wavefunction	10
2.2 Meissner effect	11
2.3 Fluxoid quantization	13

2.4	Josephson relations	14
2.5	Gauge-invariant phase difference across a junction	17
2.6	DC SQUID equation with I_c and L imbalance	18
2.7	Calculating I_{sw} using Lagrange multipliers	22
2.8	I_{sw} symmetries	23
2.9	Voltage when I exceeds I_{sw}	24
3	Methods	26
3.1	Magnetic field measurement with an unshunted DC SQUID magnetometer .	26
3.2	Fluxperiod — periodicity of the switching curve	27
3.3	Measuring I_{sw}	28
3.4	Measuring vector components of magnetic field	30
3.5	Measuring spatial variation of magnetic field	30
3.6	Multiplexing	31
3.6.1	Quietpoint — flux-bias value maximizing $ I_{sw} $	32
3.7	4-point field measurement method	33
4	Results	36
4.1	Generating a single IV curve at a single flux bias for a DC SQUID	36
4.2	I_{sw} modulation curve from many IV curves	37
4.3	I_{sw} modulation curve from raw switching events	38
4.4	Measured fluxperiods	38
4.5	Measured fields	40
5	Conclusion	42
5.1	Summary	42
5.2	Outlook	43
	Bibliography	44

List of Tables

Table 4.1	Magnetometer fluxperiods	40
Table 4.2	Initial magnetometer fields	40
Table 4.3	Final magnetometer fields	41

List of Figures

Figure 1.1	Josephson junction circuit symbol	2
Figure 1.2	The Meissner effect	3
Figure 1.3	Effects of trapped flux on a qubits	4
Figure 1.4	Effects of trapped flux on shift-register operation	5
Figure 1.5	Magnetic shielding configuration	7
Figure 1.6	DC SQUID symbol	8
Figure 2.1	London penetration depth	12
Figure 2.2	2π -periodicity of Ψ around a closed loop	13
Figure 2.3	The Josephson effect	14
Figure 2.4	DC SQUID current flow	18
Figure 2.5	Integration contour around a DC SQUID	19
Figure 2.6	Sheet current density in a wire with dimensions comparable to λ_L .	21
Figure 2.7	DC SQUID schematic bias reversal symmetry	24
Figure 2.8	DC SQUID switching curve bias reversal symmetry	25
Figure 3.1	Switching curve with $\Phi_{\text{background}}$	27
Figure 3.2	I_{sw} detection	29
Figure 3.3	Multiplexing of bias lines	31
Figure 3.4	Measuring a DC SQUID switching curve for devices with different I_c 's sharing the same current bias	32
Figure 3.5	DC SQUID switching curves for devices sharing the same current bias	33
Figure 3.6	Measuring an individual switching curve on a shared current-bias line	34
Figure 3.7	4-point-field method switching curve	35
Figure 4.1	IV vs measurement for (RO 5)	37
Figure 4.2	IV curves for (RO 5) at flux bias = 0 mA, 0.12 mA	37
Figure 4.3	IV curves vs flux bias for (RO 5)	38
Figure 4.4	Raw switching events for (RO 5)	39
Figure 4.5	Fluxperiod measurement for (RO 5)	39

List of Symbols

\hbar	Planck constant $6.626\,070\,15 \times 10^{-34} \text{ J Hz}^{-1}$
k_B	Boltzmann constant $1.380\,649 \times 10^{-23} \text{ J K}^{-1}$
μ_0	Vacuum magnetic permeability $\frac{2\alpha}{e^2} \frac{\hbar}{c} = 1.256\,637\,062\,12(19) \times 10^{-6} \text{ N A}^{-2}$
Φ_0	Magnetic flux quantum $\frac{\hbar}{2e} = 2.067\,833\,831(13) \times 10^{-15} \text{ Wb}$
Ψ	Macroscopic quantum wavefunction
n_s	Cooper pair number density
v	Cooper pair velocity
θ	Phase of the superconducting wavefunction
ϕ	Gauge-invariant phase of the superconducting wavefunction
Λ	London parameter
λ_L	London penetration depth
n_ϕ	Order parameter winding number
J_s	Supercurrent density
J_c	Critical supercurrent density
T_c	Critical temperature
B_c	Critical magnetic field
I_c	Critical current — max zero voltage current for a wire or Josephson junction
I_{sw}	Switching current — max/min zero voltage current for a DC SQUID at a given flux bias

List of Acronyms

SQUID	Superconducting Quantum Interference Device
QFP	Quantum Flux Parametron
DUT	Device Under Test
DAC	Digital-to-Analog Converter
ADC	Analog-to-Digital Converter
FLL	flux-locked loop

Chapter 1

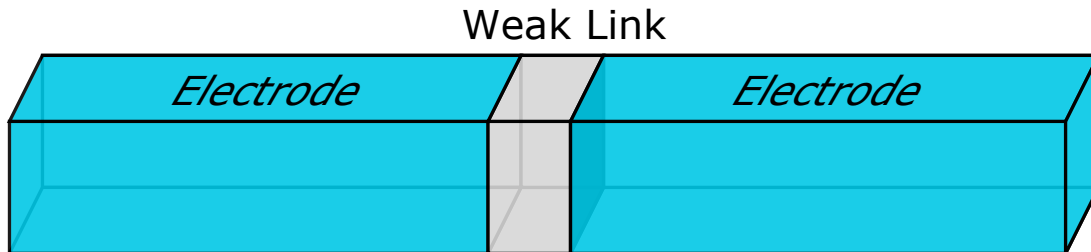
Introduction

This thesis will present techniques for making accurate absolute measurements of residual magnetic fields using a set of unshunted DC Superconducting Quantum Interference Devices (SQUIDs) to assist in low field cooling of a superconducting processor for improved operability. The structure of the thesis is as follows. This chapter will begin by motivating the use of superconductors in integrated circuits. A description of the deleterious effects that trapped magnetic flux can have on such circuits and mitigation techniques for reducing the number of trapped flux lines will follow. Chapter 2 will work through the theoretical background necessary to understand some basic properties of superconductors, Josephson junctions and devices comprised from them. This will conclude by explaining how magnetic fields affect the characteristics of an unshunted DC SQUID. Following this, Chapter 3 will detail how to use these characteristics of the SQUID to perform a magnetic field measurement. Detail will be given on the procedures necessary to measure the magnetic field when the SQUIDs are multiplexed and share signal lines. Using these methods, Chapter 4 will present the experimental results for magnetometry performed on a D-Wave Washington generation processor. Finally, Chapter 5 will discuss the work and briefly comment on the applicability of this type of measurement to other systems.

1.1 Superconducting circuits

Superconductors are best known as materials that exhibit zero DC resistance and perfect diamagnetism. Josephson junctions consist of two closely separated superconductors (see Fig. 1.1), which permits dissipationless current flow across this classically forbidden region. These and other properties of superconductors and Josephson junctions can be leveraged to make novel electronic circuits.

Some of the appealing qualities of circuits constructed out of superconducting components include extremely fast switching, with maximum clock speeds nearing the THz range [1]. The energy consumed in the switching process can be made very small [2, 3], approach-



(a) Josephson junction



(b) Circuit symbol

Figure 1.1: A Josephson junction consists of two electrodes separated by a weak link. The electrodes consist of superconducting materials (S). The weak link can be made of an insulator (I), a normal metal (N) or a constriction (C). The devices in this thesis are made with superconducting-insulator-superconducting (SIS) type junctions.

ing the Landauer limit ($k_B T \ln 2$) [4]. Improved sensitivity of sensors is achieved due to reduced thermal noise [5]. Josephson circuits are also used to define the voltage standard with quantum accuracy [6]. Additionally, the quantum mechanical nature of superconductivity can be used to open up new avenues for computing [7, 8].

1.2 Flux trapping

At low fields, superconductors exhibit perfect diamagnetism, having zero field deep in their interior. As a bulk material is cooled in a weak field, it transitions from a normal metal to a superconductor at some critical temperature. As this happens, the magnetic field in the normal region is expelled. This is known as the Meissner effect (see Fig. 1.2).

However, in the case of Type II materials and thin films of Type I superconductors the magnetic flux *can* penetrate a superconductor. This occurs when the free energy of the boundary between the normal and superconducting region is negative [9]. If the decrease in free energy from increasing the boundary is greater in magnitude than the resulting increase in free energy from decreasing the volume of the superconductor, the overall free energy of the system can be reduced by allowing a small normal region to perforate the superconducting region. Additional normal regions can be added to the bulk until it is no longer energetically favorable.

When this happens, a vortex of supercurrent will circulate around each of these normal regions. They are given the name Abrikosov vortices in bulk materials [10] and Pearl

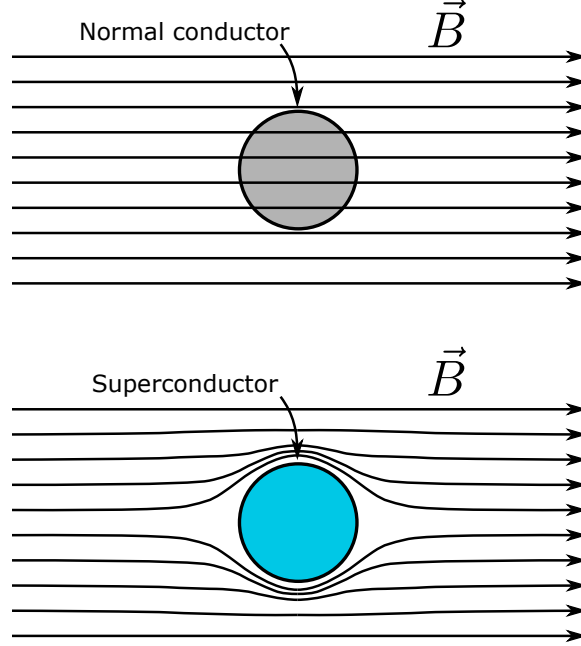


Figure 1.2: The Meissner effect. Top figure shows a material at $T > T_c$ in a magnetic field B . Bottom figure shows the material at $T < T_c$ has expelled the magnetic field from deep within its interior. This work, is a derivative of original figure by D-Wave Systems used with permission.

vortices in thin films [11], where the thickness becomes comparable to the penetration depth. Modern superconducting circuits are manufactured out of alternating thin layers of superconducting and insulating materials, thus the latter are most relevant. An alternate name is a fluxon, as the amount of magnetic flux trapped in the normal region is quantized.

Flux trapping is a stochastic process. Cooling a superconductor through its critical temperature repeatedly in the same field can result in different trapped flux configurations. However, defects in materials or grain boundaries can create preferred pinning sites.

1.3 Consequences of trapped flux in superconducting processors

Trapped flux can be beneficial and improve the critical current density (J_c) in superconductor wire [12]. In superconducting magnet applications, this results in higher magnetic fields. For circuits made up of superconducting wires and Josephson junctions, such as D-Wave processors, this is not the case. In this context, trapped flux usually degrades the operability of the circuits.

Josephson devices need to have their components manufactured within certain fabrication tolerances to achieve circuit parameters near their designed values. Failure to do

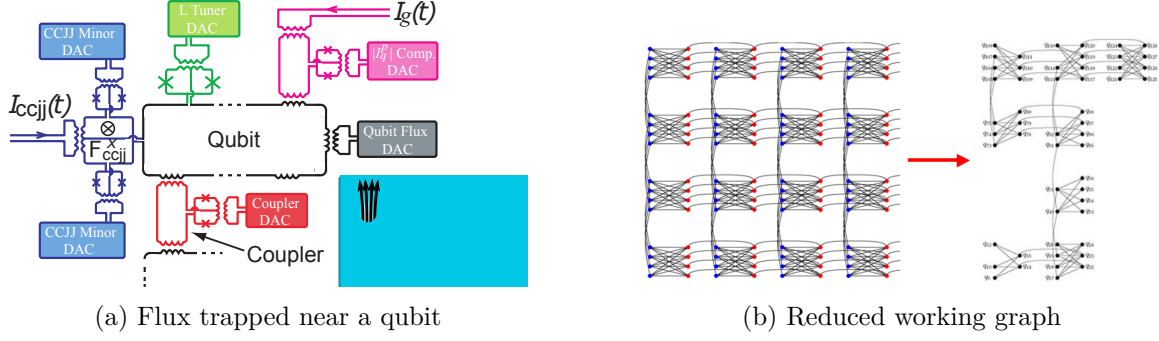


Figure 1.3: Flux trapped too close to a qubit can render it unusable. (a) A single qubit (black) and its supporting control structures (colored loops) used to control the qubit’s parameters. A nearby superconducting region (cyan) contains trapped flux lines (black arrows). If trapped flux couples too strongly to the qubit and is beyond the tuning range of the qubit flux DAC (grey), the qubit can not be used for problem solving. This work, is a derivative of original figure by D-Wave Systems used with permission. (b) A working graph consisting of qubits (dots) and the couplers (lines) connecting them. The ideal graph is shown on the left. An exaggerated working graph with qubits disabled due to trapped flux is shown on the right. This working graph results in a reduced set of problems that can be solved on the processor.

so will result in circuits that fail to perform as intended. Josephson parameters can be affected by local magnetic fields. This can be a boon, allowing tunability of individual circuit elements. But it can also be undesirable, particularly in the case where unwanted neighboring trapped flux strongly biases circuit elements. Some examples of the undesirable consequences of trapped flux for a superconducting quantum annealer are given below.

In the case of the D-Wave processors, the properties of the flux qubits [7] and their associated couplers [13] need to be controlled to both specify the computational problem and to ensure all qubits are parametrically equivalent. It is expected that different devices will have variations between their respective parameters. These variations can arise due to variations in layer thicknesses causing differences in mutual inductances between circuit elements. Another example would be differences in wire width causing variability in the inductance of the wires making up the qubits. To homogenize these properties across all devices, control structures have been used in various parts of the chip that allow tunability of those parameters. The majority of these control structures can be manipulated with local static magnetic fields provided by magnetic flux Digital-to-Analog Converters (DACs) [14, 15].

If, due to local trapped flux, the field at the device or one of its constituent control structures is larger than can be compensated by the DACs, the qubit’s properties will not be able to be homogenized with the rest of the qubits on the chip and will be unusable for computation. As a result, the number of usable devices on the chip will be reduced, limiting the size and type of problem that can be solved (see Fig. 1.3).

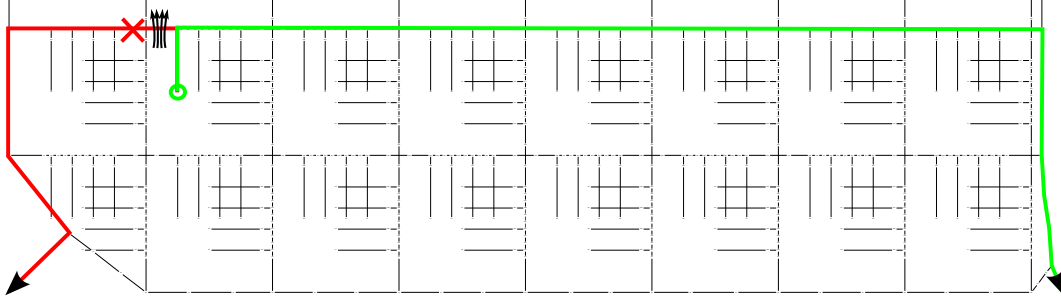


Figure 1.4: Flux trapped near a QFP shift register stage prevents data transfer. The shortest path from a qubit (green circle) to a readout readout structure (black arrow) via a QFP shift-register is indicated in red. Trapped flux lines (black arrows) prevent the nearby QFP (red x) from correctly passing its flux state to its neighbors. The qubit must be routed to an alternate readout via a longer path (green). More QFP stages need to be traversed, resulting in a longer readout time.

The flux states of the qubits at the end of the computation encode the solution of the problem being solved. These states are routed from the interior to the periphery of the processor before being transported off the chip to the room temperature electronics. This is done with the use of a Quantum Flux Parametron (QFP) shift register. The direction of the circulating current present in a QFP after annealing is determined from the magnetic field penetrating the main body. If the field is provided by the circulating current of a neighboring QFP, the opposite sign of the flux state can be copied from one QFP to another. However, flux trapped near a shift-register stage can cause a given stage to be biased towards one state regardless of the neighboring flux state. In this case, the QFP does not faithfully copy the flux state of its neighbor and data can not be passed between the two devices. To compensate for this a longer path must be taken to route this data from the source qubit to the readout structure as shown in Fig. 1.4. This leads to longer calibration times and slower computation due to the inflated readout time.

In order to maximize the number of qubits available for problem solving, and to reduce the time needed to read out the solution to a problem, the effects of flux trapped on chip must be minimized.

1.4 Minimizing the effects of trapped flux

One way to minimize the effect trapped flux has on superconducting circuitry is to ensure that flux is preferentially trapped away from flux-sensitive components. This can be done by including moating structures — holes within the large superconductor regions [16]. If these moats are sufficiently far from flux-sensitive elements, the biasing from flux trapped in them should have minimal influence on the adjacent components.

Moating structures do take up physical area. This is then area on the chip that cannot be used for circuitry. In chips using multiple superconducting layers, these moating structures would need to persist through all layers. The larger the ambient magnetic field, the larger the fraction of chip area dedicated to moating will need to be. Depending on the necessary circuit density, this can be problematic.

1.5 Minimizing the trapped flux in wires

To reduce the number of trapped flux lines within a superconducting wire, one can minimize the width of the superconducting wires. In Ref. [17], Stan et al. found that all perpendicular flux were expelled from a superconducting strip of width W below a critical field of $B = \frac{\Phi_0}{W^2}$, where Φ_0 is the magnetic flux quantum ($\frac{h}{2e} = 2.067\,833\,831(13) \times 10^{-15}$ Wb) and W is the width of the wire. This is a much larger critical field than would be expected in the bulk limit as it scales inversely with the area of the wire perpendicular to the flux. The smaller width also potentially reduces the number of pinning sites a flux line must traverse between the center of the superconducting region and the normal boundary [18].

In practice, the minimum width of the wires is set by design constraints, e.g., the minimum width and spacing the fabrication facility can reliably manufacture, or the desired inductance of a circuit component.

Though reducing the width will minimize the amount of flux trapped within the superconducting wire, many superconducting circuit components consist of loops. If the flux instead becomes trapped within or adjacent to a loop, it can still cause problems.

1.6 Minimizing the amount of trapped flux

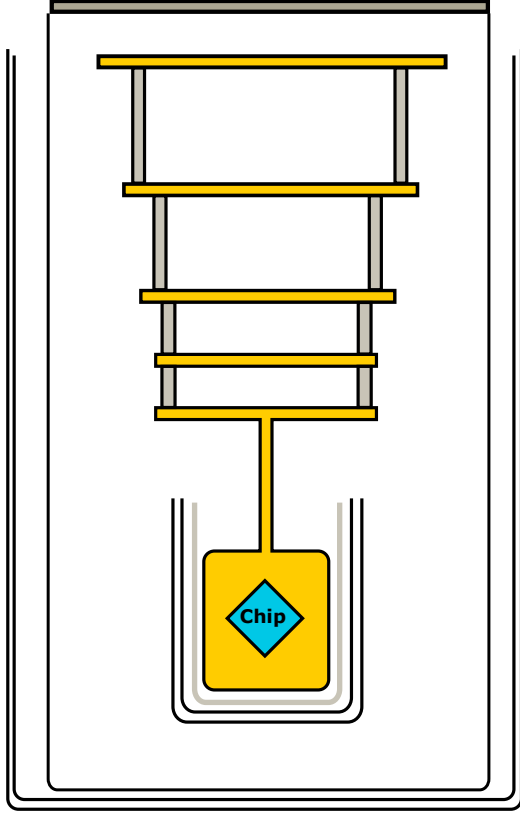
1.6.1 Low-field cooling

If the magnetic field is low when the superconducting region is cooling through its superconducting transition, there is less flux available to be trapped. With fewer trapped flux lines, less of the region needs to be reserved for moating. The circuit density can be increased or the extra space can be used to accomodate wider wires with reduced inductance.

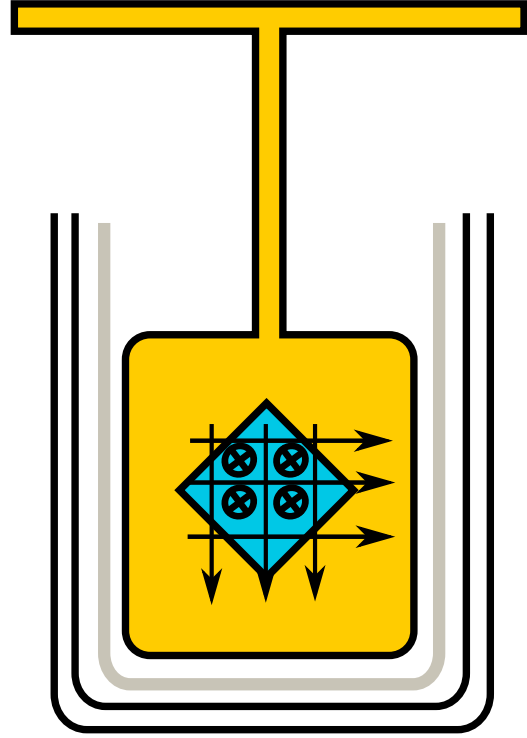
In the approximation that the processor consists of a contiguous piece of superconductor, if the magnetic flux over the area of the processor is kept below $1 \Phi_0$, no trapped flux should be possible. For a Washington processor (size $\approx 7 \text{ mm} \times 7 \text{ mm}$), this sets a reasonable upper bound for the average magnetic field across the processor area (A):

$$B_c = \frac{\Phi}{A} = \frac{\Phi_0}{4.9 \times 10^{-5} \text{ m}^2} \approx 42 \text{ pT} . \quad (1.1)$$

Achieving these low fields is done through a combination of attenuating the ambient fields and actively compensating the remaining magnetic fields (see Fig. 1.5). To attenuate



(a) Cartoon of magnetic shielding



(b) Coils supplying compensating fields

Figure 1.5: Magnetic shielding configuration (a). The two outermost open-topped cylinders (black) represent the first set of high-magnetic-permeability shields. The next cylinder (black) is the vacuum can. The thermal stages of the dilution refrigerator are shown in gold. The next two open-topped cylinders (black) represent a pair of high permeability shields thermally anchored to the mixing chamber plate. Inside those is a superconducting shield (gray) around which the compensation coils are wound. Once an acceptable flux offset configuration is achieved the system is cooled to milliKelvin temperatures for operation of the processor. This is well below the the shield's T_c , thus any change in external magnetic fields is attenuated via the Meissner effect. Inside this shield resides the sample holder (gold) and the chip (cyan). (b) shows the magnetic field (black arrows) applied by the compensation coils (not shown) in three orthogonal directions.

the fields, the processor is placed inside two concentric, room-temperature, high-magnetic-permeability shields (e.g., MuMetal). Inside those shields are two more concentric, low-temperature, high-magnetic-permeability shields.

Magnetic field is measured with DC SQUIDS located at the corners of the processor. At each location are five magnetometers: one sensitive to field in the x direction (X); one for the y direction (Y); and three for the z direction referred to by their relative pickup areas small (S), medium (M) and large (L).

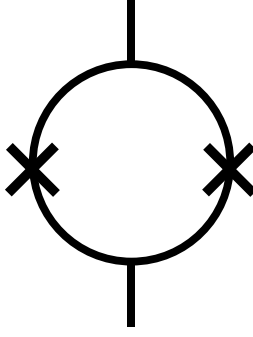


Figure 1.6: A DC SQUID is made of two parallel Josephson junctions.

The system's temperature is set to below the chip's superconducting transition temperature (9.2 K for Nb), but above the T_c of the superconducting shield. This temperature (5.16 K for the results presented in this thesis) is cold enough that the SQUIDs can operate, but warm enough that the normal superconducting shield is transparent to the compensating fields. Once the field is measured, the field is then compensated using modified Helmholtz coils for each of the x , y and z directions, which encompass the sample holder.

In this compensated field, the chip is thermally cycled up through its T_c and then back down to the previous temperature. The on-chip field is remeasured and compensated if needed. This process is repeated until the field is sufficiently small that subsequent cycles would offer no improvement. The processor is then brought to the base temperature of the dilution refrigerator for operation. If it becomes apparent that the trapped flux configuration is poor, as in the cases shown in figures 1.3 or 1.4, the process may need to be repeated until an acceptable offset configuration is achieved.

1.7 Magnetic field measurement

DC SQUIDs consist of two Josephson junctions connected in parallel as schematically shown in Fig. 1.6. The circuit is sensitive to the flux linking the loop made by the wires connecting the two junctions. This can be leveraged to perform sensitive magnetic field measurements.

1.7.1 Flux-locked loop DC SQUID

One way to measure magnetic field using a DC SQUID is to bias the SQUID with some current that exceeds the maximum zero-voltage current it can support. The average voltage across the SQUID changes as a function of the flux through the body of the SQUID and is periodic as a function of Φ_0 . Changes in flux through the body of the SQUID smaller than a Φ_0 can be detected as a change in the average voltage across the SQUID. The body

of the SQUID can be used to directly detect flux changes. A separate superconducting pick-up coil may also be used to couple flux into the body of the SQUID.

SQUIDs operated in this voltage mode are most often used in conjunction with a lock-in amplifier [9]. The lock-in amplifier provides an oscillating flux to the body of the SQUID. As a result, the average voltage across the SQUID modulates at this same frequency. The lock-in amplifier averages the voltage signal at the drive frequency. Any additional external flux linking the body of the loop, such as from a pick-up coil, shifts this lock-in-amplifier output signal. This output signal is then used in a negative feedback mode to provide a compensating flux to the SQUID, to keep the lock-in output signal fixed. The feedback is proportional to the external flux to be measured. This is referred to as a flux-locked loop (FLL). With this type of setup, sensitivities of $3.6 \text{ fT}/\sqrt{\text{Hz}}$ have been obtained [19].

1.7.2 Unshunted DC SQUID with I_{sw} modulation

The previous method of SQUID readout is not the only means for measuring magnetic field. The DC SQUID magnetometers in D-Wave processors are hysteretic and have no resistive shunt across their junctions. The property that will be modulated by the external magnetic field is the boundary separating zero-voltage and non-zero-voltage current flow. Though the achieved field sensitivities are lower in comparison to the FLL case, an unshunted DC SQUID field measurement can sometimes be preferred.

There are also situations where resistively shunting the junctions of the DC SQUID is not possible or desirable. In the case of nanoSQUIDs, the devices being manufactured are too small to include a shunt [20]. When integrated on a processor for the purpose of measuring the flux state of qubits [14], removing the shunt leaves more room for other components.

Whereas a shunted DC SQUID is constantly operated in the voltage state, the unshunted SQUID only spends a fraction of its measurement time in the voltage state. The lack of a dissipative shunt and the reduced amount of time spent in the voltage state reduces the power dissipation at the device. This can be beneficial when performing magnetic field measurements at sub-Kelvin temperatures.

As will be shown in Chapter 3, unshunted DC SQUIDs are also able to be trivially multiplexed. On circuits where input lines are at a premium, this allows more devices to be read out using fewer lines.

In the chapters that follow, I will describe techniques for measuring magnetic field using a set of integrated multiplexed unshunted DC SQUIDs.

Chapter 2

Theory

In this chapter, the necessary theoretical groundwork to understand how the magnetic field may be measured using an unshunted DC SQUID will be explained. Section 2.1 will begin with an introduction to the superconducting wavefunction and pair-velocity phase relation. This will be used to derive the Meissner effect in section 2.2, which shows that magnetic fields decay exponentially with the London penetration depth λ_L in the bulk of a superconductor. Using the Meissner effect, Section 2.3 will show that the flux contained within a ring of a thick (many λ_L) superconductor must be quantized. Section 2.4 will establish the DC Josephson effect, that a supercurrent can flow across a narrow insulating boundary and is a function of the phase drop across the junction. After some necessary bookkeeping in Section 2.5 to ensure that our phase difference is invariant under gauge transformations, all the tools are ready to describe the behavior of a DC SQUID, a loop of superconductor bisected by two Josephson junctions.

The remaining sections will investigate the behavior of the DC SQUID. Section 2.6 will give an equation for the allowed zero-voltage supercurrents that can flow across the device. Section 2.7 will show that the magnetic field through the body of the DC SQUID modulates the allowed maximum and minimum zero-voltage supercurrents. Some symmetries of this relation will then be examined to motivate a method for measuring the magnetic field that is insensitive to asymmetries between junctions and inductances of the DC SQUID.

2.1 Superconducting wavefunction

Ginsburg-Landau theory phenomenologically describes the behavior of superconductors using an order parameter that is a complex-valued wavefunction [21]. This wavefunction is not the wavefunction of an individual supercurrent carrier, but that of the coherent condensate. This macroscopic wavefunction can be derived from the microscopic theory of Bardeen-Cooper-Schrieffer (BCS) [22] and is given by

$$\Psi = \sqrt{n_s(\vec{r}, t)} e^{i\theta(\vec{r}, t)} \quad (2.1)$$

where

$$|\Psi|^2 = n_s \quad (2.2)$$

is the Cooper pair number density. For a fixed temperature and a homogeneous superconductor, n_s can be taken to be constant. As such, the dynamics of the system are governed by the $\theta(\vec{r}, t)$ term. To see how $\theta(\vec{r}, t)$ relates to circuit currents and voltages, one can follow Van Duzer [23] and first look at the expectation value of the quantum mechanical canonical momentum operator ($-i\hbar\nabla$) for this wavefunction.

$$-i\hbar\nabla\Psi = \hbar\nabla\theta\Psi \quad (2.3)$$

This describes the total momentum for the multitude of particles making up the wavefunction Ψ . The Cooper pairs share the same quantum state and thus each pair has the same momentum $p_k = \hbar\nabla\theta$.

The canonical momentum operator for a charged particle in a field is given by

$$\hat{p}_k = m\vec{v} + q\vec{A}. \quad (2.4)$$

Equating this with the momentum expectation value and rearranging terms gives

$$\nabla\theta = \frac{2m_e\vec{v}}{\hbar} - \frac{2e}{\hbar}\vec{A}, \quad (2.5)$$

the pair-velocity phase relation, where $2m_e$ and $2e$ are the mass and charge of a Cooper pair.

The current density of the superconducting pairs is

$$\vec{J}_s = -2en_s\vec{v}. \quad (2.6)$$

Substituting this into 2.5 gives

$$\nabla\theta = -\frac{2e}{\hbar}\Lambda\vec{J}_s - \frac{2e}{\hbar}\vec{A} \quad (2.7)$$

where

$$\Lambda = \frac{m_e}{2n_se^2}. \quad (2.8)$$

2.2 Meissner effect

Taking the curl of both sides of 2.7 gives

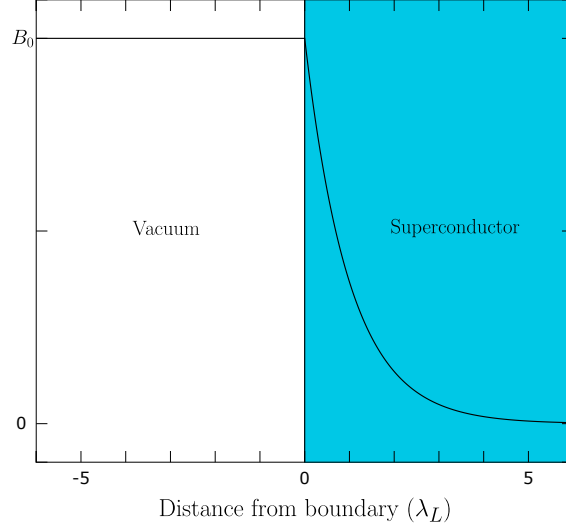


Figure 2.1: The black curve indicates the relative field strength as a function of distance from the vacuum (white)/superconductor (blue) interface.

$$\nabla \times \nabla \theta = -\nabla \times \frac{2e\Lambda \vec{J}_s}{\hbar} - \nabla \times \frac{2e}{\hbar} \vec{A}. \quad (2.9)$$

As the curl of a gradient is zero, and using $\vec{J}_s = \frac{\nabla \times \vec{B}}{\mu_0}$ and $\nabla \times \vec{A} = B$ equation 2.9 becomes

$$\nabla \times \nabla \times B = -\frac{\mu_0}{\Lambda} B. \quad (2.10)$$

From the vector identity $\nabla \times \nabla \times \vec{B} = \nabla(\nabla \cdot \vec{B}) - \nabla^2 \vec{B}$ and using $\nabla \cdot \vec{B} = 0$, we obtain

$$\nabla^2 \vec{B} = \frac{\mu_0}{\Lambda} B = \frac{1}{\lambda_L^2} B \quad (2.11)$$

where

$$\lambda_L = \sqrt{\frac{m_e}{\mu_0 n_s e^2}} \quad (2.12)$$

is the London penetration depth.

Solutions to this equation are of the form

$$\vec{B} = \vec{B}_0 e^{-x/\lambda_L}. \quad (2.13)$$

This shows that fields decrease exponentially over length scales λ_L from the edge of the superconductor (see Fig. 2.1). It also means that many λ_L from the surface, within the bulk of a superconductor, there is no magnetic field and thus $v = 0$. Or more simply stated, the majority of the supercurrent flows near the surface of the superconductor.

2.3 Fluxoid quantization

The integral of the phase gradient may be taken around a closed loop of superconductor

$$\oint \nabla \theta \cdot d\vec{\ell} . \quad (2.14)$$

The superconducting wavefunction is single-valued. As a result, the value of the wavefunction at the start and end of the integral must be the same (as shown in Fig. 2.2).

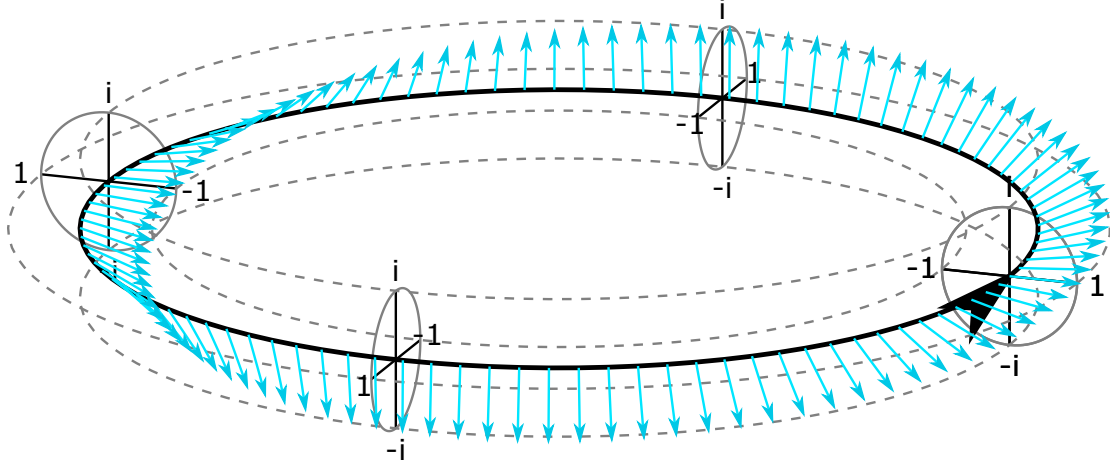


Figure 2.2: The complex phase of Ψ (blue arrows) is shown at points around a closed line integral (black circle). The phase must be the same after completing a circuit of the loop. Therefore, θ can only change by a multiple of $2\pi n_\phi$, where n_ϕ is the number times the phase has wound around the origin. For this figure, $n_\phi = 1$.

Therefore, the closed line integral must equal an integer multiple of 2π .

$$\oint \nabla \theta \cdot d\vec{\ell} = 2\pi n_\phi \quad (2.15)$$

From 2.7,

$$\oint \nabla \theta \cdot d\vec{\ell} = \oint \left(\frac{2m_e \vec{v}}{\hbar} - \frac{2e}{\hbar} \vec{A} \right) \cdot d\vec{\ell} . \quad (2.16)$$

This gives the fluxoid quantization condition

$$\oint \left(\frac{2m_e \vec{v}}{\hbar} - \frac{2e}{\hbar} \vec{A} \right) \cdot d\vec{\ell} = 2\pi n_\phi , \quad (2.17)$$

where the integral is referred to as the fluxoid.

The Meissner effect ensures that if the line integral is taken many λ_L deep within a superconductor, $\vec{v} = 0$. Combining that with 2.15 gives

$$-\frac{2e}{\hbar} \oint \vec{A} \cdot d\vec{\ell} = 2\pi n_\phi \quad (2.18)$$

The closed integral of the vector potential is just the magnetic flux linking the path. Therefore

$$\begin{aligned} -\frac{2e}{\hbar} \Phi &= 2\pi n_\phi \\ \Phi &= \frac{-\pi n_\phi \hbar}{e} \\ \Phi &= n_\phi \Phi_0 , \end{aligned}$$

which is the flux quantization condition, where the negative sign has been absorbed into n_ϕ and

$$\Phi_0 = \frac{h}{2e} = 2.067\,833\,831(13) \times 10^{-15} \text{ Wb} , \quad (2.19)$$

the magnetic flux quantum.

The end result is that the amount of magnetic flux inside a closed loop of superconductor is quantized in integer units of Φ_0 . This is the magnetic flux quantization condition.

2.4 Josephson relations

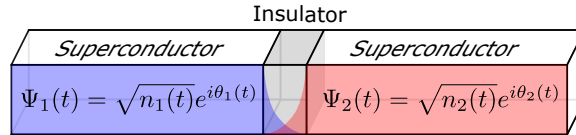


Figure 2.3: The Josephson effect. Two superconductors are connected by an insulating region (grey). The wavefunctions (blue/red) of each superconductor decay exponentially in the insulating region, but have some non-zero overlap. This allows Cooper-pair tunneling between the two superconducting regions. This work, is a derivative of original figure by D-Wave Systems used with permission.

In 1962, Josephson [24] predicted the tunneling of Cooper-pairs between superconductors separated by an insulating region. In the following section, a derivation of this result following Feynman [25] will be given. For two superconductors connected by a narrow non-superconducting region, their wavefunctions can be related as follows

$$i\hbar \frac{\partial}{\partial t} \Psi_1 = U_1 \Psi_1 + K \Psi_2 \quad (2.20)$$

$$i\hbar \frac{\partial}{\partial t} \Psi_2 = U_2 \Psi_2 + K \Psi_1 \quad (2.21)$$

K is a constant intrinsic to the junction that describes the coupling between the wavefunctions of each region. This coupling is related to the overlap of the two wavefunctions in the non-superconducting region. Assume a voltage is applied between the 2 sides

$$e^*(V_2 - V_1) = e^*V \quad (2.22)$$

$$U_2 - U_1 = e^*V \quad (2.23)$$

Take zero of energy to be the midpoint of U_1 and U_2

$$U_1 = -\frac{e^*V}{2} \quad (2.24)$$

$$U_2 = \frac{e^*V}{2} \quad (2.25)$$

$$(2.26)$$

Substitute in the wavefunctions

$$\Psi_1(t) = \sqrt{n_1(t)} e^{i\theta_1(t)} \quad (2.27)$$

$$\Psi_2(t) = \sqrt{n_2(t)} e^{i\theta_2(t)} . \quad (2.28)$$

Equation 2.20 gives

$$i\hbar \frac{\partial}{\partial t} \left[\sqrt{n_1(t)} e^{i\theta_1(t)} \right] = U_1 \sqrt{n_1(t)} e^{i\theta_1(t)} + K \sqrt{n_2(t)} e^{i\theta_2(t)} \quad (2.29)$$

$$\frac{i\hbar}{2} \frac{\partial n_1(t)}{\partial t} - \hbar n_1(t) \frac{\partial \theta_1(t)}{\partial t} = U_1 n_1(t) + K \sqrt{n_1(t) n_2(t)} e^{i[\theta_2(t) - \theta_1(t)]} . \quad (2.30)$$

$$(2.31)$$

Separating real and imaginary parts and making the substitution

$$\theta(t) = \theta_2(t) - \theta_1(t) \quad (2.32)$$

$$-\hbar n_1(t) \frac{\partial \theta_1(t)}{\partial t} = U_1 n_1(t) + K \sqrt{n_1(t) n_2(t)} \cos \theta(t) \quad (\text{Real part})$$

$$\frac{\partial \theta_1(t)}{\partial t} = \frac{e^* V}{2\hbar} + K \sqrt{\frac{n_2(t)}{n_1(t)}} \cos \theta(t)$$

$$\frac{\hbar}{2} \frac{\partial n_1(t)}{\partial t} = K \sqrt{n_1(t) n_2(t)} \sin \theta(t) \quad (\text{Imaginary part})$$

$$\frac{\partial n_1(t)}{\partial t} = \frac{2K}{\hbar} \sqrt{n_1(t) n_2(t)} \sin \theta(t) .$$

Equation 2.21 may be similarly substituted. This gives 4 coupled equations

$$\frac{\partial n_1(t)}{\partial t} = \frac{2}{\hbar} K \sqrt{n_1(t) n_2(t)} \sin \theta(t) \quad (2.33)$$

$$\frac{\partial n_2(t)}{\partial t} = -\frac{2}{\hbar} K \sqrt{n_1(t) n_2(t)} \sin \theta(t) \quad (2.34)$$

$$\frac{\partial \theta_1(t)}{\partial t} = \frac{-K}{\hbar} \sqrt{\frac{n_2(t)}{n_1(t)}} \cos \theta(t) + \frac{e^* V}{2\hbar} \quad (2.35)$$

$$\frac{\partial \theta_2(t)}{\partial t} = \frac{-K}{\hbar} \sqrt{\frac{n_1(t)}{n_2(t)}} \cos \theta(t) - \frac{e^* V}{2\hbar} . \quad (2.36)$$

$$(2.37)$$

From equations 2.34 and 2.35, we see

$$\frac{\partial n_2(t)}{\partial t} = -\frac{\partial n_1(t)}{\partial t} . \quad (2.38)$$

The rate at which pairs are depleted from the first superconductor is the same as the rate that pairs are gained in the second superconductor, so the pairs must be tunneling from one superconductor to the other. The coefficient $I_c = \frac{2}{\hbar} K \sqrt{n_1(t) n_2(t)}$ is characteristic of the junction and specifies the maximum zero-voltage current that can be passed through the junction. This gives us the DC Josephson relation. If the two regions consist of the same superconducting material and are at the same temperature then it is reasonable to assume that $n_1(t) = n_2(t)$. Taking the difference between the last two relations gives us the AC Josephson relation.

$$I(t) = I_c \sin \theta \quad (2.39)$$

$$\frac{d\theta}{dt} = \frac{2\pi}{\Phi_0} V \quad (2.40)$$

2.5 Gauge-invariant phase difference across a junction

The magnetic vector potential (\vec{A}) can have the gradient of an arbitrary scalar function added to it without changing anything physically. This occurs as part of a gauge transformation. However, this would seem to imply that the current density in equation 2.7 could take on any value. This would be unphysical. To ensure that the current density is the same irrespective of gauge, $\nabla\theta$ must change too. Define a new gauge $A \rightarrow A'$, $\theta \rightarrow \theta'$ with $A' = A + \nabla\chi$ and substitute these into equation 2.7.

$$\begin{aligned}\nabla\theta' &= \frac{2e\Lambda\vec{J}_s}{\hbar} - \frac{2\pi}{\Phi_0}(\vec{A} + \nabla\chi) \\ \nabla\theta' &= \frac{2e\Lambda\vec{J}_s}{\hbar} - \frac{2\pi}{\Phi_0}\vec{A} - \frac{2\pi}{\Phi_0}\nabla\chi \\ \nabla\theta' &= \nabla\theta - \frac{2\pi}{\Phi_0}\nabla\chi \\ \theta' &= \theta - \frac{2\pi}{\Phi_0}\chi + C\end{aligned}$$

So for the gauge $A \rightarrow A + \nabla\chi$, $\theta \rightarrow \theta - \frac{2\pi}{\Phi_0}\chi$ up to a constant, C.

Let ϕ_1 be the gauge invariant phase at point 1. The gauge-invariant phase difference follows easily.

$$\begin{aligned}\phi'_1 &= \theta_1 - \frac{2\pi}{\Phi_0}\chi_1 \\ \phi'_2 &= \theta_2 - \frac{2\pi}{\Phi_0}\chi_2 \\ \phi'_2 - \phi'_1 &= \theta_2 - \theta_1 - \frac{2\pi}{\Phi_0}\chi_2 + \frac{2\pi}{\Phi_0}\chi_1 \\ &= \theta_2 - \theta_1 - \frac{2\pi}{\Phi_0} \int_1^2 \nabla\chi \cdot \vec{d\ell}\end{aligned}$$

As $A' = A + \nabla\chi$,

$$\begin{aligned}\phi'_2 - \phi'_1 &= \theta_2 - \theta_1 - \frac{2\pi}{\Phi_0} \int_1^2 (A' - A) \cdot \vec{d\ell} \\ \phi'_2 - \phi'_1 + \frac{2\pi}{\Phi_0} \int_1^2 A' \cdot \vec{d\ell} &= \theta_2 - \theta_1 + \frac{2\pi}{\Phi_0} \int_1^2 A \cdot \vec{d\ell}.\end{aligned}$$

So the gauge-invariant phase difference

$$\phi = \theta_2 - \theta_1 + \frac{2\pi}{\Phi_0} \int_1^2 \mathbf{A} \cdot d\vec{\ell} , \quad (2.41)$$

is the same regardless of the chosen gauge function χ .

2.6 DC SQUID equation with I_c and L imbalance

A DC SQUID is a superconducting loop containing two Josephson junctions. If current is passed through both junctions of the DC SQUID, the sum of the current in the two branches must equal the total applied current. With the current flowing through each junction described by 2.39, this gives

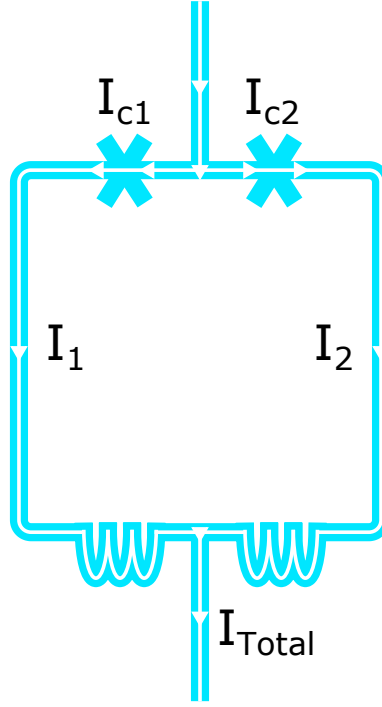


Figure 2.4: Direction of current flow in a DC SQUID. Arrows indicate direction of positive current flow in each of the superconducting regions (cyan). I_1 indicates the current through left inductive branch of the DC SQUID via the Josephson junction with a critical current I_{c1} . I_2 is the current through the right branch via Josephson junction with critical current I_{c2} . The total current is the sum of the currents through each branch $I_{\text{Total}} = I_1 + I_2$

$$I(\phi_1, \phi_2) = I_{C1} \sin \phi_1 + I_{C2} \sin \phi_2 . \quad (2.42)$$

As will now be shown, the difference between the gauge-invariant phase difference of each junction will be constrained as a function external flux (Φ_{ext}) through the body of the

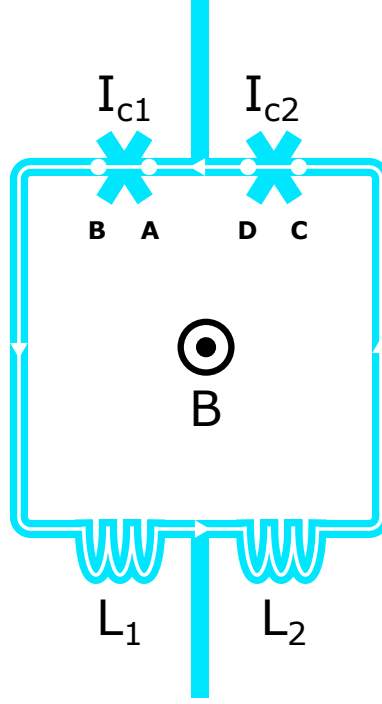


Figure 2.5: Integration contour taken around the body of a DC SQUID. Integration path is indicated by the white line and is in direction of the arrows. Integral starts and finishes at point A. B indicates the direction of the magnetic field through the body of the SQUID. L_1 and L_2 represent the geometric inductance of the branch containing the junction with the same index. The direction of positive magnetic field is taken to be out of the page as indicated by B .

DC SQUID, n_ϕ and the product of the inductance and I_c of each branch. The body of the DC SQUID is a loop. Therefore, from the fluxoid quantization condition and Fig. 2.5

$$\oint \nabla \phi \cdot d\vec{\ell} = \int_A^B \nabla \phi \cdot d\vec{\ell} + \int_B^C \nabla \phi \cdot d\vec{\ell} + \int_C^D \nabla \phi \cdot d\vec{\ell} + \int_D^A \nabla \phi \cdot d\vec{\ell} = 2n\pi. \quad (2.43)$$

Using equation 2.41 for the gauge invariant phase difference, the first term in our line integral becomes

$$\begin{aligned} \int_A^B \nabla \phi \cdot d\vec{\ell} &= \phi_B - \phi_A \\ \phi_1 &= \phi_B - \phi_A + \frac{2\pi}{\Phi_0} \int_A^B \vec{A} \cdot d\vec{\ell} \\ \phi_B - \phi_A &= \phi_1 - \frac{2\pi}{\Phi_0} \int_A^B \vec{A} \cdot d\vec{\ell}. \end{aligned}$$

Similarly, The third term of equation 2.43 can be found to be

$$\phi_D - \phi_C = -\phi_2 - \frac{2\pi}{\Phi_0} \int_C^D \vec{A} \cdot d\vec{\ell} .$$

The sign in front of the integral has changed as \vec{A} , which goes in the same direction as the current, is now in the opposite direction to $d\vec{\ell}$.

The two remaining terms, corresponding to the change of gradient in the superconductor, can be found by taking the integral of equation 2.7.

$$\int_B^C \nabla\theta = - \int_B^C \frac{2\pi}{\Phi_0} \Lambda \vec{J}_s \cdot d\vec{\ell} - \int_B^C \frac{2\pi}{\Phi_0} \vec{A} \cdot d\vec{\ell} \quad (2.44)$$

$$\int_A^D \nabla\theta = - \int_A^D \frac{2\pi}{\Phi_0} \Lambda \vec{J}_s \cdot d\vec{\ell} - \int_A^D \frac{2\pi}{\Phi_0} \vec{A} \cdot d\vec{\ell} \quad (2.45)$$

$$(2.46)$$

Substituting these terms back into equation 2.43 gives

$$\begin{aligned} \phi_1 - \phi_2 - \frac{2\pi}{\Phi_0} \int_A^B \vec{A} \cdot d\vec{\ell} - \frac{2\pi}{\Phi_0} \int_B^C \vec{A} \cdot d\vec{\ell} - \frac{2\pi}{\Phi_0} \int_C^D \vec{A} \cdot d\vec{\ell} - \frac{2\pi}{\Phi_0} \int_D^A \vec{A} \cdot d\vec{\ell} \\ - \frac{2\pi}{\Phi_0} \int_B^C \Lambda \vec{J}_s \cdot d\vec{\ell} - \frac{2\pi}{\Phi_0} \int_A^D \Lambda \vec{J}_s \cdot d\vec{\ell} = 2n\pi . \end{aligned} \quad (2.47)$$

Collecting the integrals of \vec{A} into a single closed integral yields

$$\phi_1 - \phi_2 - \frac{2\pi}{\Phi_0} \oint \vec{A} \cdot d\vec{\ell} - \int_B^C \frac{2\pi}{\Phi_0} \Lambda \vec{J}_s \cdot d\vec{\ell} - \int_A^D \frac{2\pi}{\Phi_0} \Lambda \vec{J}_s \cdot d\vec{\ell} = 2n\pi . \quad (2.48)$$

$\oint \vec{A} \cdot d\vec{\ell}$ is just the total magnetic flux linked by the loop, Φ_{Total} . This flux is the external flux linking the loop (Φ_{ext}) plus the self-induced flux in the inductors of each branch. The magnetic flux in an inductor is given by $\Phi = LI$. The current through each inductor must be the same as the current flowing through their respective junctions and can be determined by 2.39. This gives

$$\Phi_{\text{Total}} = \Phi_{\text{ext}} + L_1 I_{C1} \sin \phi_1 - L_2 I_{C2} \sin \phi_2 . \quad (2.49)$$

As stated in section 2.2, when both the thickness (d) and the width (a) of the cross-section of the wire are much greater than λ_L there exists a region within the wire where the current density is zero. In that region, the latter two integrals in Eq. 2.48 go to zero. In the case where both the thickness and width are less than λ_L , the current density takes a constant value $J_s = I/(ad)$ across the wire. If $a > d$ and $ad \gg \lambda_L^2$, as is the case for

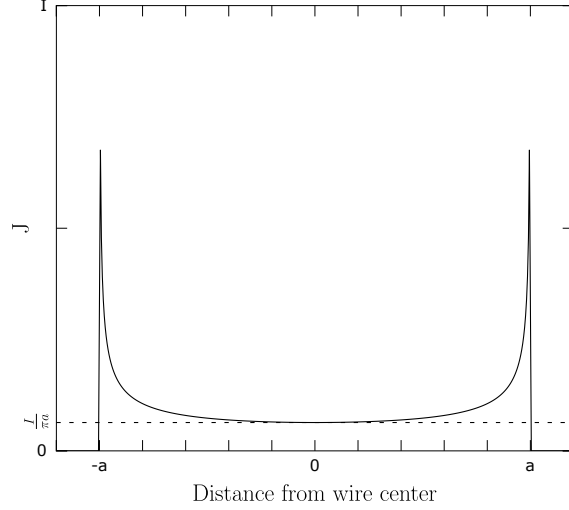


Figure 2.6: The curve marks the sheet current density averaged over the thickness of a wire where $ad \gg \lambda_L^2$. $J(0) = \frac{I}{\pi a}$ at the center of the wire.

our SQUIDS, Brandt and Indenbom [26] give an expression for the sheet current (in units A/m) as a function of the position (y) across the width of the wire

$$J(y) = \frac{I}{\pi \sqrt{a^2 - y^2}} \quad (2.50)$$

where $|y| < a$ and the sheet current has been averaged over the thickness (see Fig. 2.6). This relation will be valid as long as the applied field and current do not bring the wire close to H_{C1} at the edges of the wire. In the center of the wire ($y = 0$)

$$J_0 = \frac{I}{\pi a} . \quad (2.51)$$

Let ℓ_{BC} be the distance between points A and B and let ℓ_{DA} be the distance between D and A in the center of the wire. Substituting Φ_{Total} and the expressions for current density into equation 2.48 gives

$$\phi_1 - \phi_2 - \frac{2\pi}{\Phi_0} (\Phi_{\text{ext}} + L_1 I_{C1} \sin \phi_1 - L_2 I_{C2} \sin \phi_2) \quad (2.52)$$

$$- \frac{2\pi}{\Phi_0} \frac{\Lambda}{\pi a} \left(I_{C1} \sin \phi_1 \frac{\ell_{DA}}{2} - I_{C2} \sin \phi_2 \frac{\ell_{DA}}{2} \right) \quad (2.53)$$

$$- \frac{2\pi}{\Phi_0} \frac{\Lambda}{\pi a} \left(I_{C1} \sin \phi_1 \frac{\ell_{BC}}{2} - I_{C2} \sin \phi_2 \frac{\ell_{BC}}{2} \right) = 2n\pi . \quad (2.54)$$

So after rearranging terms, the difference between the gauge invariant phase difference across the two junctions is

$$\phi_1 - \phi_2 = 2n\pi + \phi_{\text{ext}} + \beta_1 \sin \phi_1 - \beta_2 \sin \phi_2 \quad (2.55)$$

where

$$\phi_{\text{ext}} = \frac{2\pi}{\Phi_0} \Phi_{\text{ext}} \quad (2.56)$$

$$\beta_1 = \frac{2\pi}{\Phi_0} I_{C1} \left(L_1 + \frac{\Lambda}{\pi a} \frac{\ell_{BC} + \ell_{DA}}{2} \right) \quad (2.57)$$

$$\beta_2 = \frac{2\pi}{\Phi_0} I_{C2} \left(L_2 + \frac{\Lambda}{\pi a} \frac{\ell_{BC} + \ell_{DA}}{2} \right) . \quad (2.58)$$

The term in the parenthesis for each β_i is the sum of a geometric and kinetic inductance of the respective branch.

2.7 Calculating I_{sw} using Lagrange multipliers

The current traversing the DC SQUID can now be described by equation 2.42 with the phases ϕ_1 and ϕ_2 constrained by the fluxoid quantization requirement of equation 2.55. Given these 2 equations, one can find the maximum zero-voltage current before the DC SQUID switches to the voltage state, I_{sw} . The extrema of equation 2.42 can be found by using Lagrange multipliers. Our constraint function is

$$g(\phi_1, \phi_2) = -\phi_1 + \phi_2 + 2n\pi + \phi_{\text{ext}} + \beta_1 \sin \phi_1 + \beta_2 \sin \phi_2 . \quad (2.59)$$

Subject to this constraint, the current will have extrema when

$$\frac{\partial I(\phi_1, \phi_2)}{\partial \phi_1} = \lambda \frac{\partial g(\phi_1, \phi_2)}{\partial \phi_1} , \quad \frac{\partial I(\phi_1, \phi_2)}{\partial \phi_2} = \lambda \frac{\partial g(\phi_1, \phi_2)}{\partial \phi_2} . \quad (2.60)$$

Evaluating the derivatives, we obtain

$$I_{C1} \cos \phi_1 = \lambda (-1 + \beta_1 \cos \phi_1) \quad (2.61)$$

$$I_{C2} \cos \phi_2 = \lambda (1 - \beta_2 \cos \phi_2) . \quad (2.62)$$

Equating the two expressions for λ , we have

$$\frac{I_{C1} \cos \phi_1}{(-1 + \beta_1 \cos \phi_1)} = \frac{I_{C2} \cos \phi_2}{(1 - \beta_2 \cos \phi_2)} \quad (2.63)$$

Solving for $\cos \phi_2$ gives an expression for the relationship that ϕ_1 and ϕ_2 must satisfy at I_{sw} . This gives us 3 equations that specify I_{sw}

$$I_{sw}(\phi_1, \phi_2) = I_{C1} \sin \phi_1 + I_{C2} \sin \phi_2 \quad (2.64)$$

such that ϕ_1 and ϕ_2 satisfy the constraints

$$\cos \phi_2 = \frac{I_{C1} \cos \phi_1}{-I_{C2} + (I_{C1}\beta_2 + I_{C2}\beta_1) \cos \phi_1} \quad (2.65)$$

and

$$\phi_{\text{ext}} = \phi_1 - \phi_2 - 2n\pi - \beta_1 \sin \phi_1 + \beta_2 \sin \phi_2 . \quad (2.66)$$

Here ϕ_1 and ϕ_2 are restricted to the range $-\pi$ to π .

2.8 I_{sw} symmetries

Let ϕ_1 and ϕ_2 be a set of phases that satisfies equation 2.65 and 2.66. If ϕ_{ext} is changed by a multiple of 2π , n_ϕ will change by the same multiple and ϕ_1 and ϕ_2 will be unchanged. Therefore,

$$I_{sw}(\phi_1(\phi_{\text{ext}} + 2n\pi), \phi_2(\phi_{\text{ext}} + 2n\pi)) = I_{sw}(\phi_1(\phi_{\text{ext}}), \phi_2(\phi_{\text{ext}})) \quad (2.67)$$

so I_{sw} is 2π periodic as a function of ϕ_{ext} .

For these same phases ϕ_1 and ϕ_2 , it is also clear from the even parity of the cosines in equation 2.65 that $-\phi_1$ and $-\phi_2$ will also be solutions. What happens to $\phi_{\text{ext}}(\phi_1, \phi_2)$ when the signs of ϕ_1 and ϕ_2 are swapped?

$$\begin{aligned} \phi_{\text{ext}}(-\phi_1, -\phi_2) &= -\phi_1 + \phi_2 - 2n\pi - \beta_1 \sin(-\phi_1) + \beta_2 \sin(-\phi_2) \\ &= -\phi_1 + \phi_2 - 2n\pi + \beta_1 \sin \phi_1 - \beta_2 \sin \phi_2 \\ &= -\phi_{\text{ext}}(\phi_1, \phi_2) \mod (2\pi) \end{aligned}$$

This means that changing the sign of the field in the loop is the same as changing the signs of both ϕ_1 and ϕ_2 . Seeing the effect this has on the I_{sw} of the SQUID, we find

$$\begin{aligned} I_{sw}(-\phi_1, -\phi_2) &= I_{C1} \sin(-\phi_1) + I_{C2} \sin(-\phi_2) \\ &= -I_{C1} \sin \phi_1 - I_{C2} \sin \phi_2 \\ I_{sw}(-\phi_1, -\phi_2) &= -I_{sw}(\phi_1, \phi_2) . \end{aligned}$$

Switching the polarity of the field through the body of the SQUID, switches the polarity of I_{sw} .

$$I_{sw}(\phi_{\text{ext}}) = -I_{sw}(-\phi_{\text{ext}}) \quad (2.68)$$

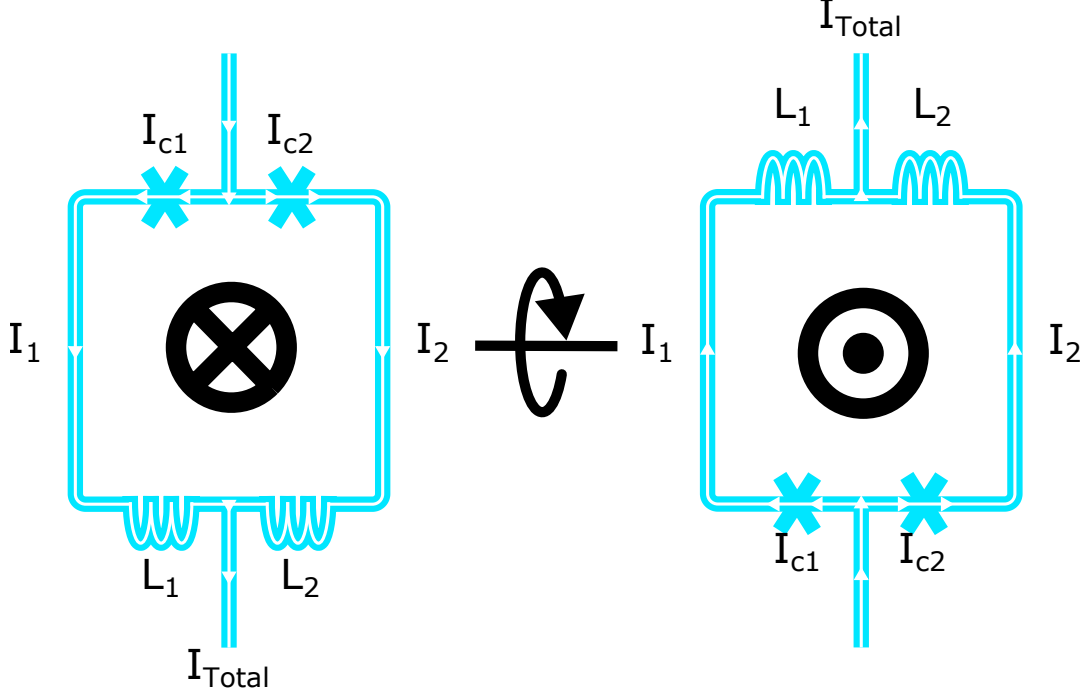


Figure 2.7: Rotating the DC SQUID about an axis perpendicular to the current flow and parallel to the pick-up area does not change any of the switching characteristics of the device. The rotated device has the opposite polarity of both the flux and the current under the original directions of positive current and flux. The magnitudes of both are unchanged. Thus $I_{sw}(\Phi_{ext}) = -I_{sw}(-\Phi_{ext})$.

This can also be seen by through a rotation of the circuit as shown in Fig. 2.7.

This symmetry can be leveraged to develop a measurement of the ϕ_{ext} of the DC SQUID that is not affected by asymmetry of the junction I_c 's or inductances. This can be seen in both Fig. 2.8a and Fig. 2.8b.

2.9 Voltage when I exceeds I_{sw}

If the current is ramped from zero to a value exceeding I_{sw} , the supercurrent will provide the current up to but not exceeding I_{sw} . The excess current through the device must be provided by quasiparticle excitations. The quasiparticle current will not start to flow until a voltage builds up exceeding $2\Delta/e$, where Δ/e is the gap-voltage at zero temperature. This spike in voltage from zero to twice the gap-voltage can be used to determine I_{sw} .

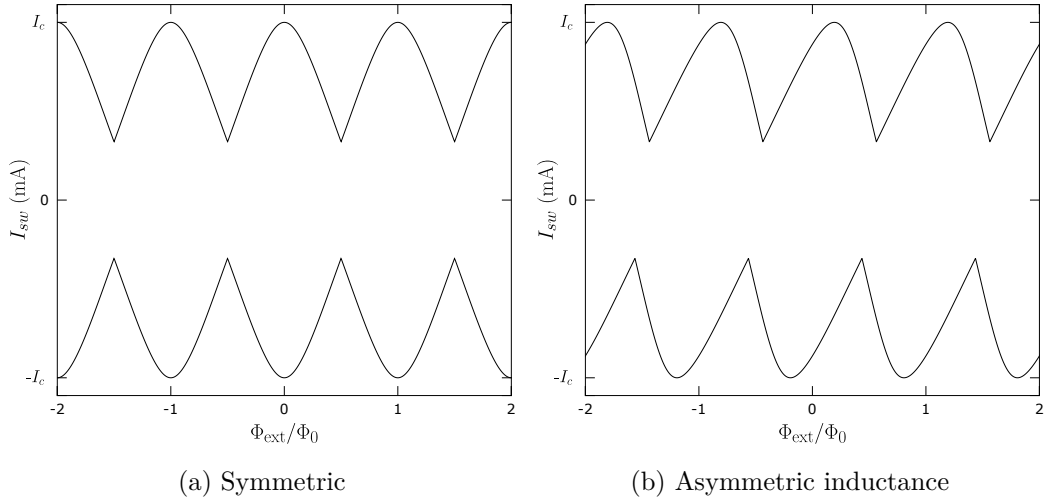


Figure 2.8: Bias reversal symmetry of I_{sw} . (a) The switching curve for a symmetric DC SQUID where $I_{C1} = I_{C2} = 0.5$ mA and $L_1 = L_2 = 0.5$ pH. (b) The effect of severe inductance asymmetry for a DC SQUID where $I_{C1} = I_{C2} = 0.5$ mA and $L_1 = 0.9$ pH, $L_2 = 0.1$ pH. The peak switching current no longer occurs when Φ_{ext} is an integer multiple of Φ_0 . $I_C = I_{C1} + I_{C2}$ for both figures. In both cases, it is clear that $I_{sw}(\Phi_{ext}) = -I_{sw}(-\Phi_{ext})$

Chapter 3

Methods

As outlined in Chapter 1, in order to maximize the performance of a superconducting processor the number of trapped flux lines in the chip must be minimized. This is done by attenuating the ambient field, measuring the attenuated field, compensating the attenuated field and finally thermal-cycling the chip through its superconducting critical temperature in this field. These steps are repeated until a sufficiently low number of offsets are reached.

Using the theory developed in Chapter 2, the methods to measure the magnetic field in 3 orthogonal directions at 4 points adjacent to the processor will be shown. First, it will be shown how to measure a full switching curve (I_{sw} vs $I_{\text{flux-bias}}$) for an individual unshunted DC SQUID. Using the periodicity and phase of the curve, we can obtain a measurement of the magnetic field perpendicular to the pick-up loop of the magnetometer. It will be subsequently shown what extra steps must be taken to measure the field of an individual device multiplexed with other devices. Lastly, leveraging the symmetries of the switching curve identified in section 2.8, a 4-point field measurement method will be described that provides a measurement of the field using far fewer points than the full switching curve and is immune to I_c or inductance asymmetries between the branches of the DC SQUID.

3.1 Magnetic field measurement with an unshunted DC SQUID magnetometer

As outlined in section 2.7, the externally applied magnetic flux through the body of a DC SQUID (Φ_{ext}) modulates the maximum and minimum zero-voltage current (I_{sw} , switching current) that the DC SQUID can support. The flux through the body of the SQUID is the sum of the background magnetic flux ($\Phi_{\text{background}}$) and the magnetic flux (Φ_{bias}) in the loop produced by a local current carrying wire (flux-bias line).

$$\Phi_{\text{ext}} = \Phi_{\text{background}} + \Phi_{\text{bias}} \quad (3.1)$$

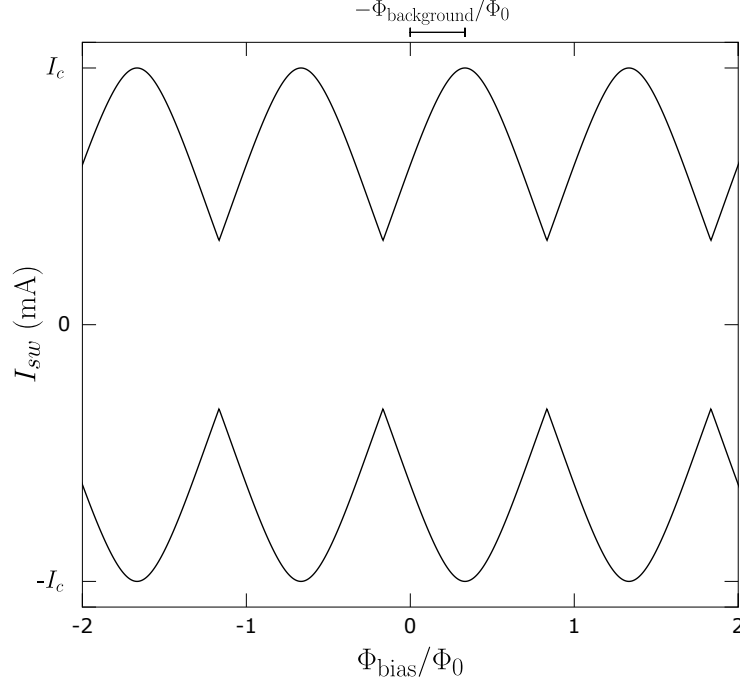


Figure 3.1: $\Phi_{\text{background}}$ shifts the phase of the switching curve.

Φ_{bias} is the magnetic flux produced in the pick-up area of the SQUID through mutual inductance M with a current carrying wire

$$\Phi_{\text{bias}} = MI_{\text{flux-bias}} . \quad (3.2)$$

Assuming a uniform field, the background magnetic field that produces $\Phi_{\text{background}}$ is given by

$$B_{\text{background}} = \frac{\Phi_{\text{background}}}{A} \quad (3.3)$$

where A is the pick-up area of the SQUID and B is the magnetic field component normal to A .

$\Phi_{\text{background}}$ can be determined by measuring I_{sw} at many $I_{\text{flux-bias}}$ to trace out the full switching curve. $\Phi_{\text{background}}$ will correspond to the phase of the switching curve as seen in Figure. 3.1. In a DC SQUID with very little I_c or inductance asymmetry, such as in Fig. 2.8a, this would correspond to the peaks of the curves being shifted to some non-zero value.

3.2 Fluxperiod — periodicity of the switching curve

As the switching curve is measured by varying $I_{\text{flux-bias}}$, the measured shift is in units of current, not flux. This shift must be converted into a magnetic flux by determining the

mutual inductance between the flux-bias line and the SQUID body. The magnetic field can then be calculated using the dimensions of the magnetometer measured.

Equation 2.67 alternatively stated in flux units shows that I_{sw} has a period of Φ_0 . Therefore, this period ($\Delta I_{\text{flux-bias}}$) is the amount of bias-line current needed to change the magnetic flux in the pick-up area of the SQUID by exactly one Φ_0 . The mutual inductance (or **fluxperiod**) is just

$$M = \frac{\Phi_0}{\Delta I_{\text{flux-bias}}} . \quad (3.4)$$

Multiplying the phase in current units by the fluxperiod gives the phase in flux units. Substituting this flux into equation 3.3 gives us the magnitude of the magnetic field perpendicular to the pick-up area of the SQUID.

Note that due to the flux periodicity of the magnetometer, there is an ambiguity as to which lobe corresponds to having zero flux in the body of each SQUID. The phase in flux units can therefore only be known modulo Φ_0 . To avoid this ambiguity, three magnetometers sensitive to magnetic fields in the z direction are used. The magnetometers are referred to by their relative pickup areas (hereafter small, medium and large), which are specifically designed to not be multiples of one another. The small, medium and large magnetometers are all located very close to each other and, as such, should be measuring similar fields. As the field is already attenuated greatly, large magnetic field gradients are not expected between nearby magnetometer locations. The pick-up areas of the small, medium and large magnetometers are $1399 \mu\text{m}^2$, $4900 \mu\text{m}^2$ and $22\,500 \mu\text{m}^2$, respectively. This corresponds to periods of 1478, 422 and 92 nT. The nearest multiple of the periods where the fields would measure within 1 nT of each other corresponds to 67 988 nT, well above the field expected in the attenuated environment. DC SQUIDs in the voltage state with different periodicities have also been used to increase dynamic range [27].

Fields larger than the sensitivity of any particular magnetometer can be measured by determining how many flux quanta must be present in each magnetometer for all three magnetometers to agree on the field that is present. In the majority of cases, we are trying to minimize the field, so this is not necessary. In rare cases where magnetic components have found their way onto the sample holder, this technique has proved useful for quantifying large fields.

3.3 Measuring I_{sw}

I_{sw} is the current bias at which the DC SQUID switches from the zero voltage state. The current at which this transition occurs may be measured by monitoring the voltage across the DC SQUID while the current bias is increased. For these hysteretic DC SQUIDs, the SQUID will stay in the voltage state until the current is ramped down close to zero.

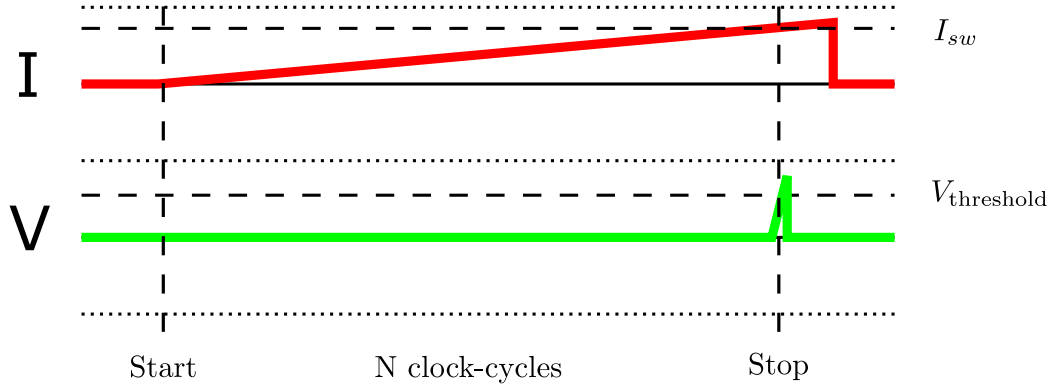


Figure 3.2: I_{sw} detection using a voltage comparator. The applied current (top) and voltage (bottom) across the current-bias line of a SQUID are shown. Clock cycles are counted from the start of the current ramp. As the current is ramped, a voltage comparator monitors the voltage across the current-bias line. When the voltage exceeds $V_{\text{threshold}}$, the voltage comparator signals for the counting to stop. I_{sw} is the applied current present when the counting stopped.

Although I_{sw} could be obtained by measuring the full IV curve and sifting through the data to find where the transition occurs, a hardware solution can be used to simplify and speed up this process.

In this method, the current is ramped using a piece-wise linear waveform specified by (time, current) pairs. The clock-cycle for the electronics is 20 ns. A counter enumerates how many clock-cycles have passed since the beginning of the waveform. A voltage comparator monitors the voltage across the DC SQUID and outputs a digital pulse when the voltage exceeds a threshold set close to $2\Delta/e$ (2.7 mV for Nb). The counter stops counting when this pulse is received. The switching current can be determined by interpolating the current that was present in the waveform after the measured number of cycles as shown in Fig. 3.2. One measurement gives an estimate of I_{sw} for the given flux bias.

If this measurement is repeated several times at the same flux bias, a Gaussian distribution of switching events is revealed. The broadening is due to the thermal escape of the DC SQUID into its voltage state [28]. These events are converted into a single uncertain number described by the mean and standard error of the events.

This process can then be repeated for both polarities of the current ramp and for many different flux-bias values to determine the full I_{sw} vs flux bias curve. From this switching curve, the features of interest for magnetometry can be determined such as the flux bias that maximizes or minimizes I_{sw} , the periodicity of switching curve, or the phase of the curve from which the magnetic field can be determined. Additional DC SQUID circuit-parameters may also be characterized (see [29], [30]).

3.4 Measuring vector components of magnetic field

The D-Wave quantum annealing processor consists of multiple metal layers. Although the majority of the loops in on-chip devices lie in the chip plane and as such are most sensitive to fields oriented normal to the chip plane (z direction), the connections between the wiring layers will form loops sensitive to parallel field. The body of the wires connecting adjacent layers (vias) can also trap flux. For this reason, it is necessary to measure and compensate the magnetic field in the 2 directions (x and y directions) orthogonal to the chip normal direction as well.

To make a pick-up loop sensitive to fields in the x and y directions, a pickup loop can be wound from the top-most wiring layer to the bottom-most wiring connected by vias traversing the interstitial layers. The sectional area for the x and y directions is small compared to the z direction. A single loop might therefore not provide enough flux sensitivity. The pickup area can be increased by a multiple of the original loop area by helically winding additional loops. In practice, this is done until enough sensitivity is achieved.

3.5 Measuring spatial variation of magnetic field

The amount of flux that can be trapped on the chip is related to the total flux through the processor. It is insufficient to measure the field components at a single point. If the field were measured at a single point, no gradient information about the field would be obtained. One could end up in a situation where the field measured at the sensor is low, but the field present at the chip is substantially larger.

The interior of the chip is reserved for processor circuitry, but magnetometer packages can be placed around the periphery. At each of the four corners of the processor a magnetometer package is placed consisting of the five aforementioned DC SQUIDS types. Three DC SQUIDS have pickup loops sensitive to fields normal to the chip plane (z direction), but with different pickup areas (small, medium, large). The other two DC SQUIDS consist of loops sensitive to fields in the chip plane and are orthogonal to each other (x and y directions).

From the four magnetometer packages, a rough map of the spatial variation of the field is obtained. In cases where a gradient is observed, the gradient can be compensated with gradient coils. On systems without gradient coils, the magnitude of the field at every point on the chip is minimized. This is done by minimizing the average of the fields measured at the four corners. This is the equivalent of setting the field at the center of the chip to zero field assuming only a field offset and linear gradients in the x and y directions.

As the DC SQUIDS are integrated on-chip with the processor, one obtains excellent spatial resolution of the field present near the processor. Additionally, the orthogonality of the DC SQUIDS sensitive to different orientations is set by the orthogonality of the

deposited metal layers. Other methods for measuring orthogonal field components using DC SQUIDs would consist of using three separate chips oriented (almost) orthogonal to each other [31]. The wiring of integrated magnetometers is much easier.

3.6 Multiplexing

Each DC SQUID requires a current-bias and flux-bias line to be operated. Individually addressing the magnetometers would require $4 \text{ packages} \times 5 \text{ DC SQUIDs} \times 2 \text{ bias lines per SQUID} = 40 \text{ bias lines}$. Fortunately, the magnetometer signal lines can be multiplexed to read all 20 SQUIDs using far fewer lines.

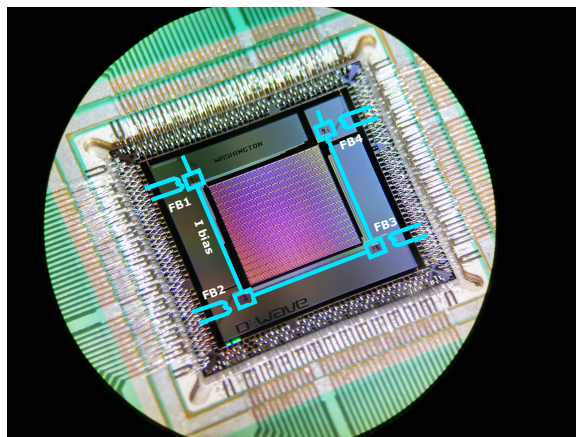


Figure 3.3: Multiplexing of current-bias and flux-bias lines. A magnetometer package resides at each of the corners of Washington generation processors. Each package contains one of each type of magnetometer (S , M , L , X and Y). Magnetometers of the same type, but in different packages (blue squares) share a common I_{bias} . The flux-bias lines (FB1-FB4) are shared amongst the 5 magnetometer types within each package. This work, is a derivative of original figure by D-Wave Systems used with permission.

As shown in figure 3.3, devices of the same direction and sensitivity (S , M , L , X or Y) share current-bias lines and devices in the same magnetometer package share flux-bias lines. For a ramp on a given current-bias line, the switching event measured will always be from the device with the lowest I_{sw} . When modulating the flux bias of a Device Under Test (DUT), this switching event will be from the DUT as long as the I_{sw} of the DUT is less than the maximum I_{sw} of all other devices on the current-bias line. If there are significant flux offsets in the other devices or they have smaller junction I_c 's, the switching curve can contain switching events from devices other than the DUT. This is undesirable.

In order to avoid erroneous switching events while measuring the fluxperiod for a device, the data are trimmed in two regions prior to fitting. A percentage of the points taken around the peak I_{sw} are discarded as the maximum I_{sw} observed will be that of the device with the lowest I_{sw} . If said device's I_{sw} is sufficiently lower than the DUT, the peak I_{sw} region

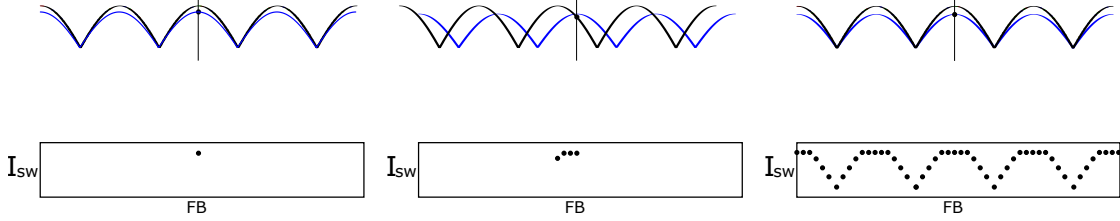


Figure 3.4: (Top) shows the overlaid switching curves for the SQUIDs. The blue device has a smaller I_c . (Bottom) shows recorded I_{sw} vs flux bias points for the DUT, where time is increasing from the left to the right graphs. (Top left) Shows that as the current is ramped, the low I_c device switches (black dot) first rather than the DUT. (Top center) Shows that this continues until the DUT (black) is flux biased such that its I_{sw} is smaller. The DUT's full switching curve has a plateau near its peak (bottom right). This, however, does not inhibit the ability to measure the phase or the fluxperiod of the DUT.

of the DUT will have a plateau at the I_{sw} of the smaller I_{sw} device (see Fig. 3.4). These are not switching events corresponding to the I_{sw} of the DUT and are discarded. If the comparators are improperly tuned, the initial switch to the voltage state can be missed. Escape from features in the subgap region can subsequently trigger the comparator. One such feature is when the Josephson oscillations match the resonant frequency of the DC SQUID body. This is analogous to Fiske-like resonant modes in long junctions [32, 33]. To avoid these sub-gap features, points measured around $\Phi_0/2$ applied flux bias are removed. After those points are discarded the fluxperiod is extracted from the fit. This is only done once per cooldown, as the fluxperiod is the mutual inductance between the flux-bias line and the body of the DC SQUID and should not change with time.

3.6.1 Quietpoint — flux-bias value maximizing $|I_{sw}|$

To ensure that the majority of the switching events are from the DUT, the rest of the devices sharing the same current bias must be flux biased such that they will switch at their maximum I_{sw} . This bias point corresponds to where the device will be quiet (switch the fewest number of times) while the DUT is modulated. This "**quietpoint**" can be found by measuring the switching curve of the devices without any flux bias applied to other devices. Even if part of the switching curve obtained contains some switching events from the neighbors, one should still be able to determine the quietpoint. The quietpoint value may be refined by iterating through all devices on the current-bias line while updating their quietpoints. Even in the worst case where all devices are biased exactly at their minimum respective I_{sw} , the individual quietpoint may still be found by adding a random quietpoint per device and iterating until the real quietpoints are found. This quietpoint will stay valid as long as the background magnetic field stays the same. If it is changed due to the application of the compensating fields it will need to be remeasured.

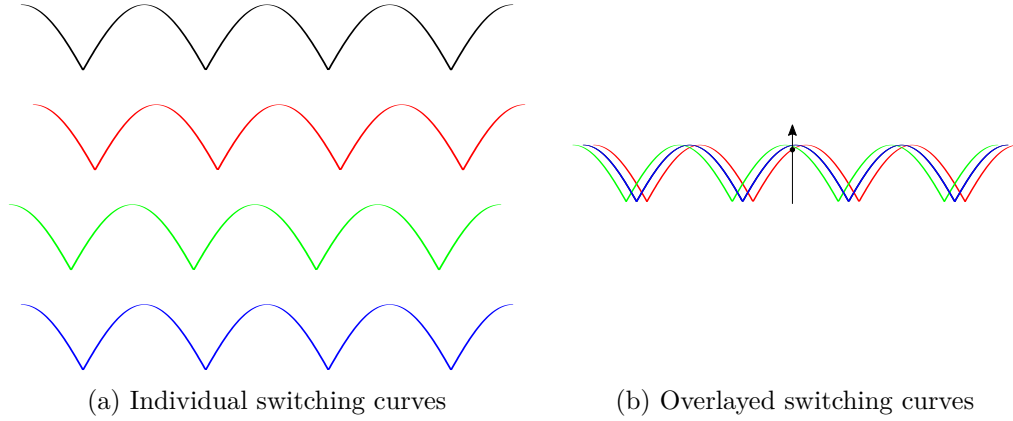


Figure 3.5: (a) Shows the switching curves (black, red, green and blue lines) for 4 DC SQUIDs. The red and green curves represent SQUIDs that have a small flux offset. (b) Shows the overlay of the switching curves for the same 4 devices, when they are connected in series on a common current-bias line. When the current is increased (black line), a voltage spike is seen when the current exceeds (black circle) the I_{sw} of any of the 4 devices.

The full switching curve for each device may now be obtained. Variations in I_c between devices means that the maximum I_c that can be measured is limited by the device with the smallest I_c on the current-bias line. This means that peak I_{sw} may be unable to be measured for a device. However, for magnetic field measurement the fluxperiod and the phase are the most important parameters and those can be determined easily. Using this XY addressing scheme, all devices can be measured sequentially using only 5 current-bias lines + 4 flux-bias lines = 9 lines. This is a great improvement.

3.7 4-point field measurement method

The field is determined by measuring the phase of the switching curve and using the fluxperiod and pickup area to convert from phase to field. From the symmetries of the DC SQUID equations, it was shown that when the sign of the phases across both junctions are reversed (by reversing the sign of the flux through the loop), the sign of the I_{sw} is reversed as well.

This symmetry can be leveraged to perform a faster measurement of the phase. The magnetometer is flux biased symmetrically some $\delta\Phi$ about the guess of the phase and current is ramped in opposite directions to measure each I_{sw} as shown in figure 3.7. For these magnetometers, this $\delta\Phi$ is chosen to be 1/4 of the fluxperiod. The sum of the I_{sw} gives a non-zero value when the guess is incorrect. To avoid incorrect measurements due to voltage offset on the current bias line, current ramps of opposite polarity for the same two flux biases are performed. The difference of the sums will be zero when the correct phase

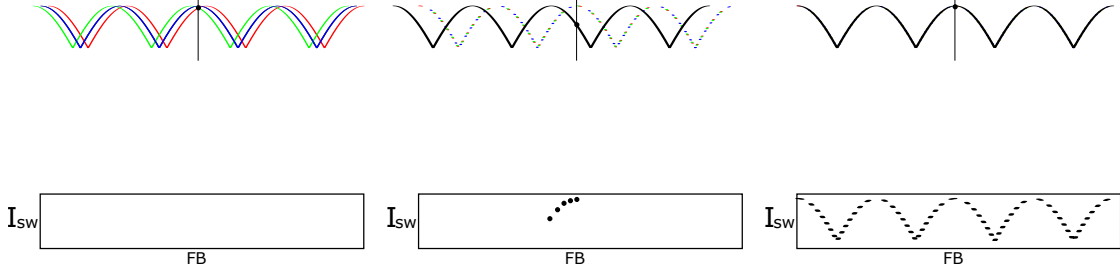


Figure 3.6: (Top) shows the overlaid switching curves for 4 SQUIDs sharing a common current-bias line at their respective flux biases. (Bottom) shows recorded I_{sw} vs flux bias points for the DUT, where time is increasing from the left to the right graphs. (Top left) Shows the overlay of all the switching curves for all devices with no applied flux bias. Offset curves (red and green) are due to local fields. (Top center) Shows the switching curves of all but the DUT (black solid curve) flux biased to their respective quietpoints (red, blue, green dotted curves). The DUT is flux biased away from its quietpoint as the current is ramped (black line). The I_{sw} at this flux bias is where the current intersects the DUT's switching curve (black circle). This I_{sw} point is the left-most point of the bottom center graph. Measurements are continued until the full switching curve for all flux-bias settings are obtained (bottom right).

guess is chosen. A zero-finder using Brent's root-finding method [34] is used to find the correct phase to the desired precision.

Whereas many flux biases would be needed to obtain the switching curve for the device, only two flux-bias values with two current ramps are needed here. As a result, with the same number of measurements, this method can be used to obtain higher precision.

Measuring the full modulation curve also requires sampling points in flux-bias regions that would be discarded prior to fitting or in regions where the change in I_{sw} vs flux bias is not steep. With the 4-point method, bias regions can be chosen where the slope is steepest and avoids problematic switching events from the regions previously mentioned in Sec. 3.6. Furthermore, this method is immune to both I_{sw} and L asymmetries within the device under test.

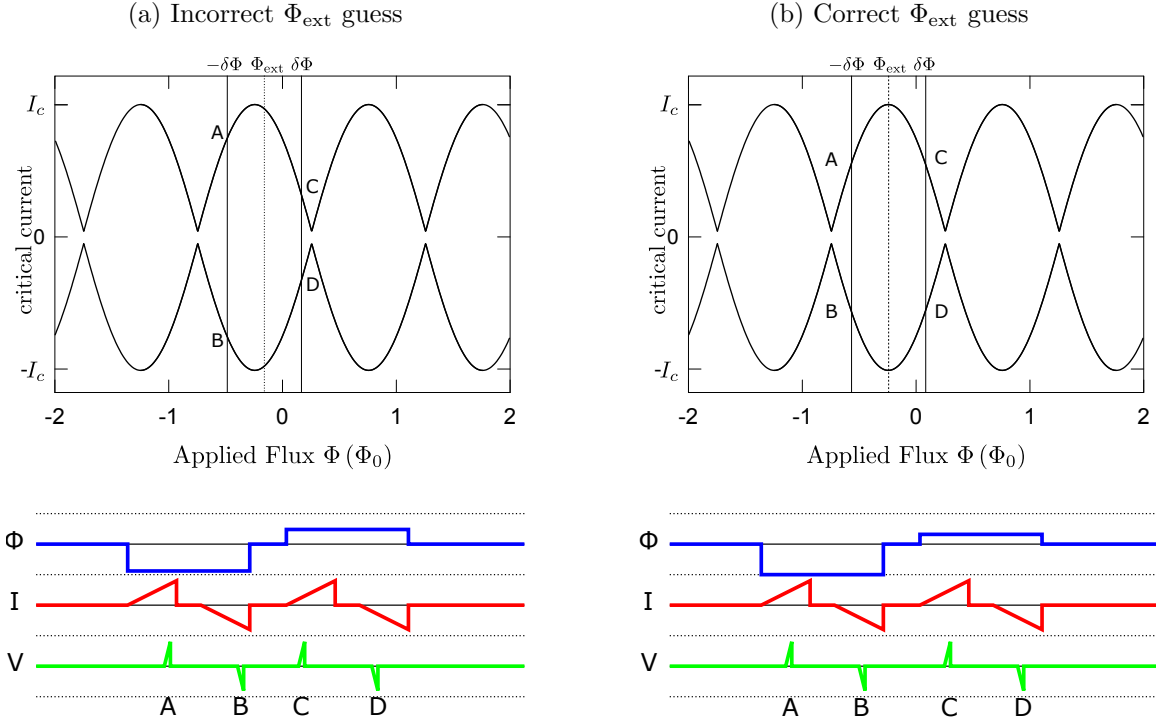


Figure 3.7: 4-point-field method switching curve for an incorrect (a) and correct (b) guess of Φ_{ext} . (Top) Shows switching curves for the DUT in the presence of a non-zero $\Phi_{\text{background}}$. (Bottom) Shows the flux bias (Φ) and current bias (I) and measured voltage (V) vs time. In each figure, current is ramped at a fixed rate in the negative and positive directions from zero while the flux is biased at $\pm\delta\Phi$ (solid lines) about some guess of Φ_{ext} (dotted line). A voltage spike is produced when the current ramp exceeds $I_{sw}(\Phi)$. In the top figures, this is the intersection (points A-D) of the current-bias sweep (solid lines) with the DUT's switching curve (solid curves). For the correct guess (b), these voltage spikes occur the same amount of time after the beginning of the individual current ramps. For the incorrect guess (a), these times differ.

Chapter 4

Results

The methods developed in Chapter 3 have been used to perform a magnetic field measurement using four magnetometer packages on a Washington generation chip, the results of which are described in this chapter. First a full IV curve for a magnetometer will be presented. Following that, measurements of multiple IV curves will be shown at various flux-bias values to demonstrate the modulation of I_{sw} . A similar measurement will then be presented, but only measuring the I_{sw} value with a voltage comparator. These results will be fit to obtain the fluxperiod for each magnetometer. Finally, the 4-point field method was used to obtain a field measurement for each of the magnetometers. This field was compensated resulting in the final field at which the chip was thermal-cycled.

4.1 Generating a single IV curve at a single flux bias for a DC SQUID

An IV curve was obtained for the magnetometer (RO 5) by applying a current and measuring the voltage across the two leads as seen in figure 4.1. This was an L magnetometer with effective pick-up area $22\,500\,\mu\text{m}^2$ located in the Northeast corner of the chip. The temperature of the dilution refrigerator as read by a calibrated Lakeshore Cernox resistance thermometer was 5.16 K. The current was linearly ramped from zero to $4\,\mu\text{A}$ then down to $-4\,\mu\text{A}$ finally finishing back at zero. At each of the 200 current points the voltage was sampled with an Analog-to-Digital Converter (ADC) 128 times.

Plotting the current versus voltage, the transition between the zero-voltage and voltage state is easily distinguishable. As seen in Figure 4.2, the transition from zero-voltage current to non-zero-voltage current happens at different current values for different flux biases.

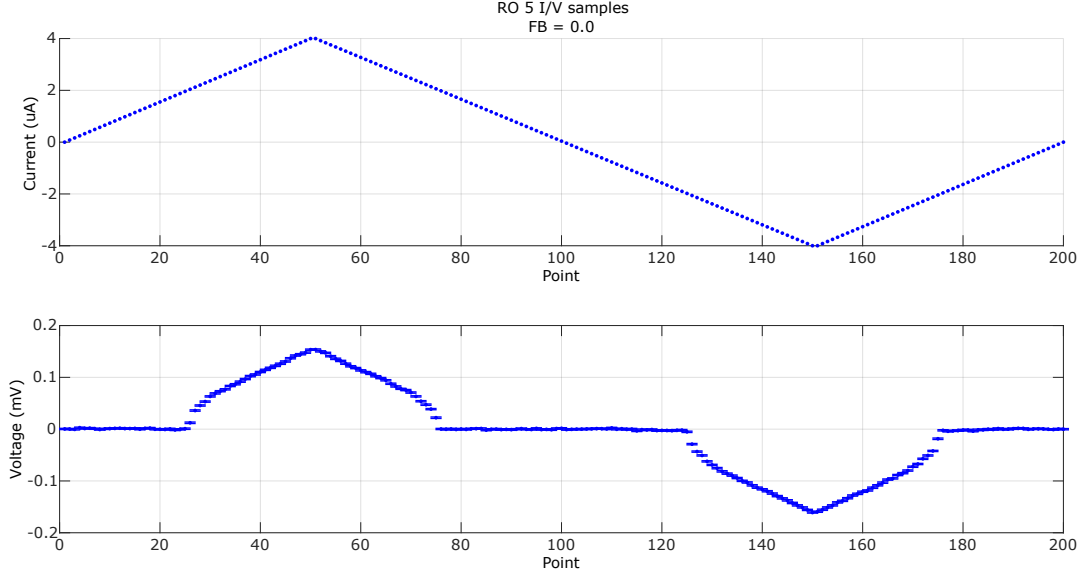


Figure 4.1: Current and Voltage versus measurement number for (RO 5) at zero flux bias. The top plot shows the 200 current values that were applied as a function of the measurement index. The bottom plot shows the mean of the 128 voltage measurements performed at each current setting. Error bars indicate one standard error.

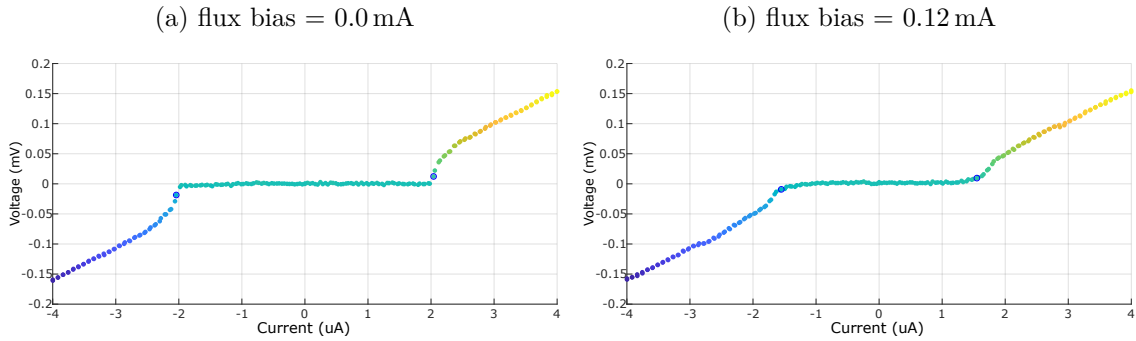


Figure 4.2: IV curve for (RO 5) at flux bias = 0 mA (a) and flux bias = 0.12 mA (b). Points are colored by their voltage. Circled points indicate the first smallest magnitude current where a non-zero voltage is seen in the positive and negative current sweep directions.

4.2 I_{sw} modulation curve from many IV curves

By taking an IV curve for many different flux-bias values, the full I_{sw} modulation curve can be made. Figure 4.3 shows the result of many IV curves taken for (RO 5) at various flux-bias values.

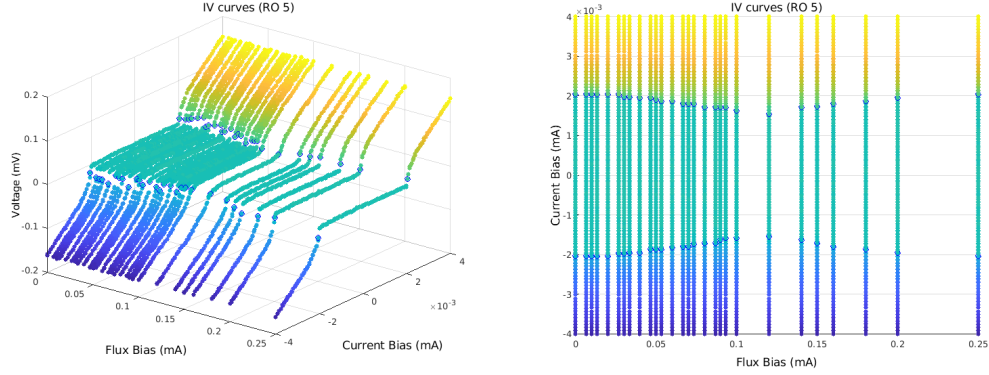


Figure 4.3: (a) 3D plot of multiple IV curves with different flux biases for (RO 5). Points are colored by the measured voltage. The transition from the zero-voltage current plateau to the voltage region is indicated by the blue circles. (b) Same data is plotted as a surface plot. The periodic modulation of I_{sw} can be seen clearly.

With this method, more data points are taken than are needed. To obtain the switching curve, only the points demarcating the boundary between the zero-voltage and voltage states are needed.

4.3 I_{sw} modulation curve from raw switching events

Following the method described in Section 3.3, a voltage comparator was used to measure just I_{sw} at each of the flux biases. The current was ramped from zero to $3\mu\text{A}$ with a ramp time of $10\mu\text{s}$.

4.4 Measured fluxperiods

This much faster method for measuring the switching events for each readout was then employed to measure the switching curve for readout. The measurement was performed twice. The first measurement obtained a reasonable estimate of the quietpoint for each device. The second measurement obtained the datapoints necessary to fit to a symmetric DC SQUID model with self-induced flux. Figure 4.5 shows the data and fit of the measurements used to obtain the fluxperiod for (RO 5).

The fluxperiod for all of the magnetometers was measured and is shown in Table 4.1. Now that the fluxperiods have been measured, the phase of each of the devices can be measured and converted into a magnetic field.

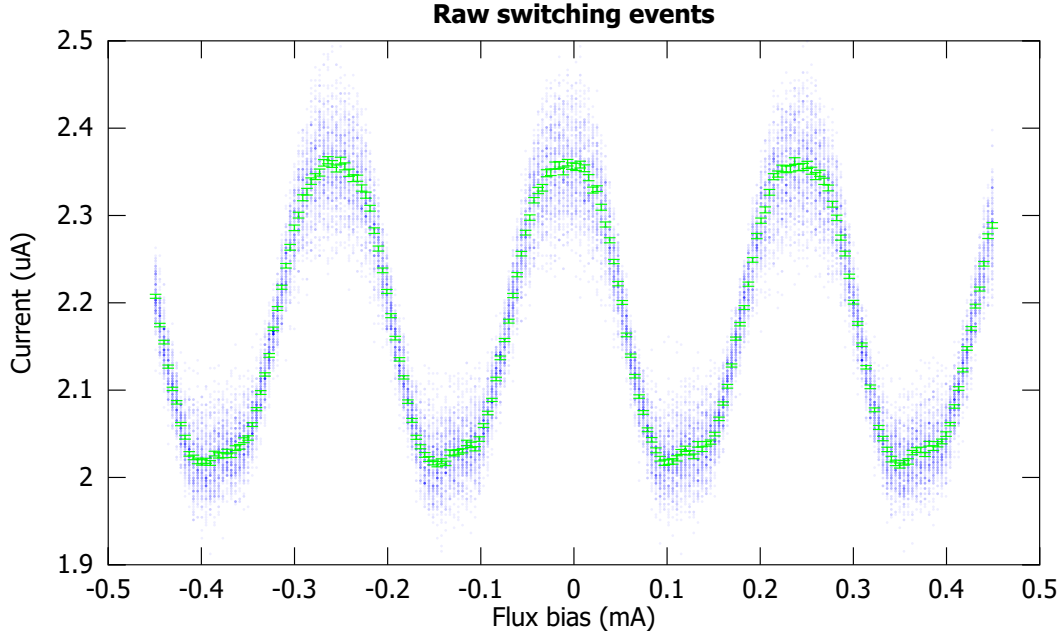


Figure 4.4: Raw switching events for (RO 5). 128 Switching events (blue dots) were measured at each of the 200 flux biases. Mean of all the switching events for a given flux bias are shown in green. Error bars indicate one standard error.

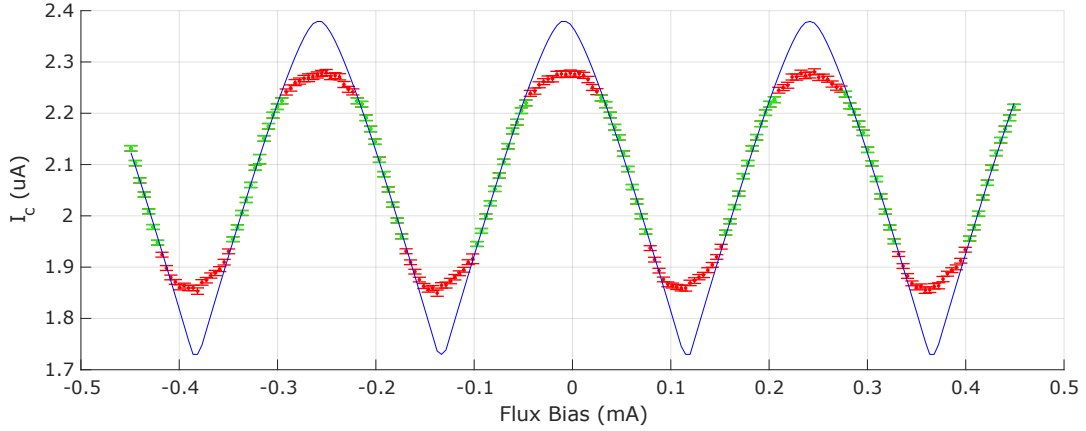


Figure 4.5: Fluxperiod measurement for RO 5. Points used for the fit are in green. Points discarded from the fit are in red. Fit is indicated with the solid blue line. Fit parameters are fluxperiod = $2.4968 \times 10^{-1} \pm 8 \times 10^{-5}$ mA/ Φ_0 , offset = $-8.49 \times 10^{-3} \pm 9 \times 10^{-5}$ μ A, $I_{sw,max} = 2.381 \pm 2 \times 10^{-3}$ μ A and $L = 479 \pm 4$ pH with a reduced $\chi^2 = 1.71$. Data was taken with a current ramp time of 100 μ s.

	Magnetometer Package location			
TYPE	Northwest	Northeast	Southwest	Southeast
S	3.67e-1	3.66e-1	3.64e-1	3.66e-1
M	2.63e-1	2.63e-1	2.61e-1	2.62e-1
L	2.46e-1	2.50e-1	2.47e-1	2.49e-1
X	3.34e-1	3.33e-1	3.29e-1	3.31e-1
Y	3.35e-1	3.33e-1	3.31e-1	3.31e-1

Table 4.1: All magnetometer fluxperiods. Fluxperiods are given in units of mA/Φ_0 .

4.5 Measured fields

The magnetic field for each device was measured using the 4-point method. The device was read 2048 times at each of the four flux-bias current-polarity settings. The phase guess was updated and more measurements were taken until the phase was known to better than the desired precision. The precision requested for the S , M and L magnetometers was 100 pT. The X and Y precision requested was 200 pT.

	Magnetometer Package location			
TYPE	Northwest	Northeast	Southwest	Southeast
S	-5.64 \pm 6e-2	-3.81 \pm 9e-2	-4.55 \pm 4e-2	-2.11 \pm 6e-2
M	-4.62 \pm 3e-2	-3.35 \pm 3e-2	-3.78 \pm 4e-2	-1.55 \pm 3e-2
L	-4.63 \pm 1e-2	-3.18 \pm 2e-2	-3.86 \pm 1e-2	-1.33 \pm 2e-2
X	-4.7 \pm 2e-1	-6.3 \pm 2e-1	-12.0 \pm 2e-1	-10.5 \pm 1e-1
Y	12.4 \pm 2e-1	11.7 \pm 1e-1	8.6 \pm 2e-1	6.6 \pm 2e-1

Table 4.2: Magnetometer fields after initially reaching a temperature of 5.16 K. Fields are given in nT.

As can be seen from Table 4.2, the initial fields for the L magnetometers were better than 5 nT in the z direction with an average of -3.249 nT with a standard error of 8 pT. At this time, magnetic field was minimized by using the compensating coils. The chip was then thermal-cycled through its superconducting transition temperature. This process was repeated 3 times for this chip until the final magnetic field values in Table 4.3 were reached. The average z field was able to be improved to 88 pT with a standard error of 8 pT. This was deemed low enough and the chip taken to base temperature for calibration.

	Magnetometer Package location							
TYPE	Northwest		Northeast		Southwest		Southeast	
S	-1.834	$\pm 9.8\text{e-}2$	-0.127	$\pm 9.2\text{e-}2$	-1.026	$\pm 9.4\text{e-}2$	1.758	$\pm 6.1\text{e-}2$
M	-1.397	$\pm 3.3\text{e-}2$	0.240	$\pm 2.8\text{e-}2$	-0.511	$\pm 4.1\text{e-}2$	1.843	$\pm 3.5\text{e-}2$
L	-1.288	$\pm 1.5\text{e-}2$	0.221	$\pm 1.8\text{e-}2$	-0.602	$\pm 1.5\text{e-}2$	2.018	$\pm 1.7\text{e-}2$
X	6.09	$\pm 1.9\text{e-}1$	3.37	$\pm 1.9\text{e-}1$	-4.76	$\pm 1.8\text{e-}1$	-3.74	$\pm 1.9\text{e-}1$
Y	4.37	$\pm 1.9\text{e-}1$	2.46	$\pm 1.9\text{e-}1$	-2.01	$\pm 1.7\text{e-}1$	-4.71	$\pm 1.7\text{e-}1$

Table 4.3: All magnetometer fields after compensation and thermal-cycling. Fields are given in nT

Chapter 5

Conclusion

5.1 Summary

Circuits leveraging the unique properties of superconducting materials and Josephson devices continue to improve. Increasing material critical temperatures and advances in cryocooler technologies make it easier to reach superconducting temperatures. As superconducting circuits grow larger and more complex, limiting the effects of flux trapping will continue to be a concern.

Low-field cooling is one method for limiting the number of trapped flux lines. Ideally, the magnetic flux should be kept below a Φ_0 across the area of the chip. The flux is reduced through a combination of passive attenuation and active field compensation. Passive attenuation is achieved using high-magnetic-permeability and superconducting shielding. Active compensation is achieved by measuring the attenuated field with on-chip magnetometers and compensating with magnetic coils.

In this thesis, the measurement of the magnetic field using sets of on-chip multiplexed unshunted DC SQUIDs was demonstrated. This was done using a set of magnetometers able to measure the field at each of the four corners of the processor. The field was measured by determining the shift in the I_{sw} modulation curve, which marks the boundary of zero-voltage current flow. This shift was converted into a field given the dimensions of the magnetometers.

The field from each magnetometer was measured serially as required by the multiplexed devices. Magnetometers were flux biased at their "quietpoint", the bias at which the magnitude of their respective switching currents were maximized. Thus, these devices would not switch while measurements of the device under test were being performed.

To measure the switching curve of an individual device, the current across the device was ramped until the appearance of a voltage spike above some threshold was seen. A 4-point method for measuring the field using far fewer flux-bias settings was developed and was shown to be immune to asymmetries in the DC SQUID. This was possible by leveraging the

symmetries intrinsic to the equations that govern DC SQUID behavior. These symmetries were shown to be valid even when the dimensions of the wires of the SQUID were on the order of a few London penetration depths.

The initial average z field across a processor was measured to be -3.249 nT with a standard error of 8 pT. After repeated thermal cycles and compensation, the average z field was able to be improved to 88 pT with a standard error of 8 pT.

5.2 Outlook

DC SQUIDs are some of the most sensitive ammeters and flux sensors available. The measurement methods described in this thesis were specific to the use of unshunted SQUIDs for the detection of flux. This was preferred for the ease of multiplexing, the use of low-frequency lines, the simplicity of the electronics used to perform the measurements and the compatibility of integration on the D-Wave processor. These benefits were deemed to outweigh the cost of slower operation than FLL methods.

This style of measurement could benefit other areas of research where the use of a shunting resistors is undesirable. NanoSQUIDs use SQUIDs manufactured with dimensions on the order of a few hundred nanometers to measure the properties of magnetic nanostructures deposited directly onto the surface of the SQUID. Reducing the size further could make it hard to include a shunting resistor. If the measurements are to be performed at sub-Kelvin temperatures, forgoing a shunt would also reduce the power dissipated at the device.

Bibliography

- [1] W. Chen, A. V. Rylyakov, Vijay Patel, J. E. Lukens, and K. K. Likharev. Rapid single flux quantum T-flip flop operating up to 770 GHz. *IEEE Transactions on Applied Superconductivity*, 9(2):3212–3215, 1999.
- [2] Oleg A. Mukhanov. Energy-efficient single flux quantum technology. *IEEE Transactions on Applied Superconductivity*, 21(3):760–769, 2011.
- [3] Naoki Takeuchi, Yuki Yamanashi, and Nobuyuki Yoshikawa. Energy efficiency of adiabatic superconductor logic. *Superconductor Science and Technology*, 28(1):015003, 2014.
- [4] Rolf Landauer. Irreversibility and heat generation in the computing process. *IBM Journal of Research and Development*, 5(3):183–191, 1961.
- [5] Joel N. Ullom and Douglas A. Bennett. Review of superconducting transition-edge sensors for x-ray and gamma-ray spectroscopy. *Superconductor Science and Technology*, 28(8):084003, 2015.
- [6] B. Jeanneret and S. P. Benz. Application of the Josephson effect in electrical metrology. *The European Physical Journal Special Topics*, 172(1):181–206, 2009.
- [7] R. Harris, J. Johansson, A. J. Berkley, M. W. Johnson, T. Lanting, Siyuan Han, P. Bunyk, E. Ladizinsky, T. Oh, I. Perminov, et al. Experimental demonstration of a robust and scalable flux qubit. *Physical Review B*, 81(13):134510, 2010.
- [8] Edward Farhi, Jeffrey Goldstone, Sam Gutmann, and Michael Sipser. Quantum computation by adiabatic evolution. *arXiv preprint quant-ph/0001106*, 2000.
- [9] John R. Waldram. *Superconductivity of metals and cuprates*. CRC Press, 2017.
- [10] A. A. Abrikosov. The magnetic properties of superconducting alloys. *Journal of Physics and Chemistry of Solids*, 2(3):199–208, 1957.
- [11] J. Pearl. Current distribution in superconducting films carrying quantized fluxoids. *Applied Physics Letters*, 5(4):65–66, 1964.
- [12] Michael Tinkham. *Introduction to superconductivity*. Courier Corporation, 1996.
- [13] R. Harris, A. J. Berkley, M. W. Johnson, P. Bunyk, S. Govorkov, M. C. Thom, S. Uchaikin, A. B. Wilson, J. Chung, E. Holtham, et al. Sign-and magnitude-tunable coupler for superconducting flux qubits. *Physical Review Letters*, 98(17):177001, 2007.

- [14] M. W. Johnson, P. Bunyk, F. Maibaum, E. Tolkacheva, A. J. Berkley, E. M. Chapple, R. Harris, J. Johansson, T. Lanting, I. Perminov, et al. A scalable control system for a superconducting adiabatic quantum optimization processor. *Superconductor Science and Technology*, 23(6):065004, 2010.
- [15] Paul I. Bunyk, Emile M. Hoskinson, Mark W. Johnson, Elena Tolkacheva, Fabio Altomare, Andrew J. Berkley, Richard Harris, Jeremy P. Hilton, Trevor Lanting, Anthony J. Przybysz, et al. Architectural considerations in the design of a superconducting quantum annealing processor. *IEEE Transactions on Applied Superconductivity*, 24(4):1–10, 2014.
- [16] Vasili K. Semenov and Mikhail M. Khapaev. How moats protect superconductor films from flux trapping. *IEEE Transactions on Applied Superconductivity*, 26(3):1–10, 2016.
- [17] Gheorghe Stan, Stuart B. Field, and John M. Martinis. Critical field for complete vortex expulsion from narrow superconducting strips. *Physical Review Letters*, 92(9):097003, 2004.
- [18] Eric Bronson, Martin P. Gelfand, and Stuart B. Field. Equilibrium configurations of Pearl vortices in narrow strips. *Physical Review B*, 73(14):144501, 2006.
- [19] D. Drung, C. Abmann, J. Beyer, A. Kirste, M. Peters, F. Ruede, and Th. Schurig. Highly sensitive and easy-to-use SQUID sensors. *IEEE Transactions on Applied Superconductivity*, 17(2):699–704, 2007.
- [20] Wolfgang Wernsdorfer. From micro-to nano-SQUIDs: applications to nanomagnetism. *Superconductor Science and Technology*, 22(6):064013, 2009.
- [21] V. L. Ginzburg and L. D. Landau. On the theory of superconductivity, zh. lksper. Teoret. Fiz, 20:1064–1082, 1950.
- [22] Lev Petrovich Gorâkov. Microscopic derivation of the Ginzburg-Landau equations in the theory of superconductivity. *Sov. Phys. JETP*, 9(6):1364–1367, 1959.
- [23] Theodore Van Duzer and Charles William Turner. Principles of superconductive devices and circuits. 1981.
- [24] Brian David Josephson. Possible new effects in superconductive tunnelling. *Physics Letters*, 1(7):251–253, 1962.
- [25] R. Feynman, R. Leiton, and M. Sends. The Feynman Lectures on Physics. Vol. 3. Quantum Mechanics (Part 1), 1967.
- [26] Ernst Helmut Brandt and Mikhail Indenbom. Type-II-superconductor strip with current in a perpendicular magnetic field. *Physical Review B*, 48(17):12893, 1993.
- [27] T. Schönau, M. Schmelz, V. Zakosarenko, R. Stolz, M. Meyer, S. Anders, L. Fritzsche, and H. G. Meyer. SQUID-based setup for the absolute measurement of the Earth’s magnetic field. *Superconductor Science and Technology*, 26(3):035013, 2013.
- [28] Carlo Cosmelli, Pasquale Carelli, Maria Gabriella Castellano, Fabio Chiarello, Roberto Leoni, and Guido Torrioli. A hysteretic DC SQUID reading the flux states of an RF SQUID. *IEEE Transactions on Applied Superconductivity*, 11(1):990–993, 2001.

- [29] R. L. Peterson and Clark A. Hamilton. Analysis of threshold curves for superconducting interferometers. *Journal of Applied Physics*, 50(12):8135–8142, 1979.
- [30] E. O. Schulz-DuBois and P. Wolf. Static characteristics of Josephson interferometers. *Applied Physics*, 16(4):317–338, 1978.
- [31] T. Schönau, V. Zakosarenko, M. Schmelz, R. Stolz, S. Anders, S. Linzen, M. Meyer, J. W. E. Faßbinder, and H. G. Meyer. Absolute calibration of a three-axis SQUID-cascade vector magnetometer. *Measurement Science and Technology*, 28(1), 2017.
- [32] Antonio Barone and Gianfranco Paterno. *Physics and Applications of the Josephson effect*. Wiley, 1982.
- [33] Gross, Rudolf and Marx, Achim. Applied Superconductivity: Josephson Effect and Superconducting Electronics. https://www.wmi.badw.de/teaching/Lecturenotes/AS/AS_Chapter3.pdf, 2009. Online; accessed 29-August-2019.
- [34] Richard P. Brent. An algorithm with guaranteed convergence for finding a zero of a function. *The Computer Journal*, 14(4):422–425, 1971.